

Mainshock rupture properties, aftershock activities and remotely triggered seismicity associated with the 2025 Mw7.7 Sagaing fault earthquake in Myanmar



Zhigang Peng^{a,*}, Xinglin Lei^b, Dun Wang^c, Xu Si^a, Phuc Mach^a, Qiu Zhong^d, Chang Ding^a, Yangfan Deng^e, Min Qin^f, Suqiu Miao^f

^a School of Earth and Atmospheric Sciences Georgia Institute of Technology, Atlanta, 30332, United States

^b Institute of Geology, China Earthquake Administration, Beijing, 100029, China

^c Chinese University of Geosciences, Wuhan, Hubei, 430074, China

^d Guangdong Earthquake Agency, Guangzhou, 510070, China

^e Guangzhou Institute of Geochemistry, Chinese Academy of Sciences, Guangzhou, 510640, China

^f Yunnan Earthquake Agency, Kunming, 650224, China

ARTICLE INFO

Keywords:

Sagaing fault
2025 Myanmar earthquake
Supershear rupture
Remote triggering
Fault zone head waves
Bimaterial interface

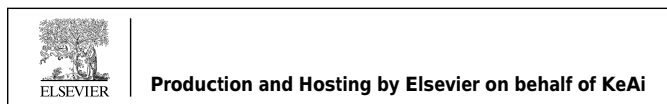
ABSTRACT

A devastating Mw 7.7 earthquake struck near Mandalay, Myanmar, on March 28, 2025, causing extensive damage and casualties across Myanmar and neighboring regions. The 2025 event occurred in a well-recognized seismic gap along the Sagaing Fault. Here we focus on the mainshock rupture properties based on back-projection of teleseismic P waves and early aftershock locations, analysis of near-field seismic recordings for the mainshock initiation, and remotely triggered seismicity following the Mw7.7 mainshock. We find that the ~500 km mainshock rupture can be revealed by both rapid back-projection of teleseismic P waves from multiple broadband arrays and early aftershock locations within about 3 h from the Thai Meteorological Department (TMD) catalog. The rupture speed went supershear in the southward propagation after the initial bilateral subshear ruptures, as expected for large strike-slip earthquakes of such sizes. Clear fault zone head waves that are reflected along a bimaterial fault interface are observed at the only near-fault station GE.NPW on the slower side about 2.6 km away from the Sagaing fault, consistent with the preferred direction of a supershear rupture propagating to the south. In addition, aftershocks from the regional TMD catalog appear to be located mostly to the east of the mainshock rupture. While we cannot completely rule out mis-locations from the one-sided station distribution, these off-fault seismicity could also be explained by reactivations of subsidiary faults within the Shan Plateau, or an eastward dipping of the mainshock rupture plane. Although no immediate foreshocks were found from several nearby stations, we identify one sub-event with magnitude ~6 at the beginning of the mainshock with a slightly different focal mechanism about 20–30 km south of the hypocenter determined by the United States Geological Survey (USGS). The mainshock also occurred when the tidal stresses reached its maximum on the right-lateral strike-slip fault, likely indicating that the timing of the mainshock is modulated by the solid earth tides. We find a significant increase of seismic activity near the Thailand/Myanmar border, in multiple (geothermally active) regions of Yunnan province in Southwest China, as well as the Xingfengjian reservoir in the Guangdong province in South China. Because static stress changes from the mainshock are small but negative near the Thailand/Myanmar border, the occurrence of microseismicity in this and other regions can be mainly explained by remote triggering from dynamic stress changes of the mainshock rupture. Our analyses

* Corresponding author.

E-mail address: zpeng@gatech.edu (Z. Peng).

Peer review under the responsibility of Editorial Board of Earthquake Research Advances.



<https://doi.org/10.1016/j.eqrea.2025.100413>

Received 25 May 2025; Received in revised form 4 August 2025; Accepted 13 August 2025

2772-4670/© 2025 China Earthquake Networks Center. Publishing services by Elsevier B.V. on behalf of KeAi Communications Co. Ltd. This is an open access article under the CC BY-NC-ND license (<http://creativecommons.org/licenses/by-nc-nd/4.0/>).

demonstrate the importance of rapid analysis on openly available seismic data and catalog to better understand the rupture properties and triggered seismicity following large earthquakes.

1. Introduction

On March 28th, 2025, a moment magnitude (Mw7.7) earthquake nucleated near Mandalay, the second largest city in Myanmar. The mainshock propagated predominately along the Sagaing Fault to the south for about 100 s (Hubbard and Bradley, 2025; Goldberg et al., 2025; Wei et al., 2025; Xu et al., 2025a, 2025b, 2025c), resulting in significant damages and casualties in Myanmar and neighboring countries such as Thailand and China (Shahzada et al., 2025). The Sagaing Fault is a major ~1400-km-long fault, which accommodates the right-lateral motions between the India-Australia and the Eurasian plates (Tun and Watkinson, 2017). It connects the divergent plate boundaries in the Andaman Sea and the active collision fronts near the Eastern Himalayan Syntaxis (EHS) in the Tibetan Plateau and hosted multiple Mw \geq 6 earthquakes over the past centuries (Wang et al., 2014).

This M7.7 event is the largest strike-slip earthquake ever occurred in this region in the past 100 years. While initial finite-fault waveform modeling from the United States Geological Survey (USGS) indicated a mainshock rupture length of around 250 km (Hubbard and Bradley, 2025; Cai et al., 2025), subsequent analysis (Antoine et al., 2025; Bradley and Hubbard, 2025; Goldberg et al., 2025; Melgar et al., 2025; Vera et al., 2025; Wei et al., 2025; Xu et al., 2025a, 2025b, 2025c; Inoue et al., 2025; Ye et al., 2025; Zhao et al., 2025) based on aftershocks from finite-fault inversion, back-projection of teleseismic P waves, sub-event analysis, InSAR data, optical satellite imagery and other remote sensing analysis all suggested a much longer surface rupture of 450–500 km. Long-period coda wave analysis revealed that the moment magnitude Mw of this event is 7.86 (Li and Song, 2025), consistent with its ultra-long rupture. Here we use the Mw = 7.7 determined by the USGS for the rest paper.

Resolving the rupture length shortly after a large earthquake like this event helps to determine the places with the strongest shaking (Wald et al., 2022) and subsequent rescue efforts. In addition, it provides robust input for subsequent analysis of the unbroken segment and future seismic hazard in the surrounding region (Toda and Stein, 2025; Li et al., 2025). In this article, we present additional evidence for a simple and long surface rupture, including its supershear rupture properties, which is expected for large strike-slip earthquakes (Robinson et al., 2010; Wang et al., 2016b; Ren et al., 2024; Yao and Yang, 2025). In addition, we include detailed analysis on the aftershock distributions, Coulomb stress changes due the mainshock, tidal modulations of the mainshock occurrence times, initiations of the mainshock ruptures and widespread remote triggering in South and Southeast Asia following the mainshock.

2. Tectonic background

While the central section of the Sagaing Fault that hosted the recent M7.7 earthquake (termed the Sagaing Fault earthquake in this study) is relatively simple, the tectonic environment in a broader context is rather complex (Fig. 1a). The India-Australia plate moves northward to collide with the Eurasia plate, creating the Himalayan Mountain Front and the Tibetan plateau (Yin and Harrison, 2000). At its eastern edge of the plate boundary, motion between the two plates is highly oblique, which is accommodated by the Indo-Burma subduction zone (IBSZ), the Sagaing Fault and other strike-slip faults in the Indo-Burma area (Fig. 1a). Further south, such an oblique motion is accommodated by the Sumatra-Andaman subduction zone and the Great Sumatran fault (McCaffrey, 2009). In between these active faults lies the Burma microplate, which is a small tectonic plate located between the Indian and the Sunda Plates, accommodating complex interactions such as

oblique subduction, strike-slip motion, and back-arc spreading deformation in the eastern Indian Ocean region (Gahalaut and Gahalaut, 2007).

The Sagaing Fault is the dominant tectonic feature in Myanmar (Tun and Watkinson, 2017), which separates the Central Myanmar Basin (CMB) to the west and the Shan Plateau to the east (Fig. 1). Further to the west of the CMB lies the Indo-Burma Mountain Range (IBMR), generally interpreted as the accretionary wedge due to the IBSZ. The IBMR (and to a less degree the Sagaing Fault) shows a convex shape westward towards the Bengal basin, likely due to combined effects of the buttressing to the north by the Shillong Plateau and the EHS (Nielsen et al., 2004), and the westward crustal flow related to the Tibet Plateau collapse (Rangin et al., 2013). Geodetic measurements revealed ~18–22 mm/year of dextral strike-slip motion along the Sagaing Fault (Wang et al., 2014; Mallick et al., 2019; Lindsey et al., 2023). Stress inversions from focal mechanisms of moderate-size earthquakes in this region revealed that the maximum horizontal compressive stress direction is in the NE-SW (Hu et al., 2017; Timsina et al., 2024).

The Sagaing Fault has long been recognized as one of 11 “earthquake fault superhighways”, where continental strike-slip faults with very long and straight segments (Robinson et al., 2010). It is very close to several major cities (e.g., Mandalay, the capital Naypyidaw, and Yangon), and has hosted more than 10 M6+ earthquakes in the past centuries (Fig. 1b). Among them, the 1839 Ava earthquake (M7.9-8.3) likely ruptured a similar segment when comparing with the most recent M7.7 event (Wang et al., 2014; Hubbard and Bradley, 2025). The northern end of the M7.7 event (~22.5 deg) appeared to stop at the Singu Plateau (also known as Letha Taung), a small basaltic plateau that are offset by the Sagaing Fault (Tun and Watkinson, 2017). It also partially overlaps with the southern end of the 2012 M6.8 Thabeikkyin earthquake (Wei et al., 2025), and possibly the 1946 Mw7.7 (Ms7.8) earthquake (Antoine et al., 2025). The southern end of the M7.7 event (~18 deg) appears to be close to or overlaps with the M7.3 earthquake in 1930 (Wang et al., 2014; Hubbard and Bradley, 2025; Wei et al., 2025). Coulomb stress transfer calculations from 10 M > 6.5 earthquakes along the Sagaing Fault (Xiong et al., 2017) also showed that most subsequent events occurred in the positive stress increase section following the previous events, and the central and southern section is due for a large earthquake. In this perspective, this M7.7 event is well expected (Hubbard and Bradley, 2025), because it occurred in a seismic gap (Mogi, 1979; Jackson and Kagan, 2001; Kagan et al., 2012) where significant slip of ~4 m (as expected from the mean slip rate) has accumulated in the past few centuries without any major earthquakes releasing the tectonic strain.

3. Mainshock rupture properties from back-projection analysis

We apply a back-projection method (Wang et al., 2011; Wang et al., 2016a; Kiser and Ishii, 2017) to image the rupture process of the 2025 Myanmar earthquake using teleseismic data recorded by regional arrays in Europe, Alaska, and Australia (Fig. 2a). The employed method corrects the Doppler effect caused by variations in the source rupture location. To depict the primary and credible rupture features, we plot the locations of the maximum energy points (Fig. 2). These three regional arrays (Europe (EU), Australia (AU) and Alaska (AL)) are located to the northwest, southeast, and northeast of the epicenter, respectively, with epicentral distances ranging from 30° to 90°, which is the optimal range for teleseismic P-wave back-projection (Kiser and Ishii, 2017).

The back-projection results from the three arrays show that the primary fault involved in this earthquake was the Sagaing Fault. The

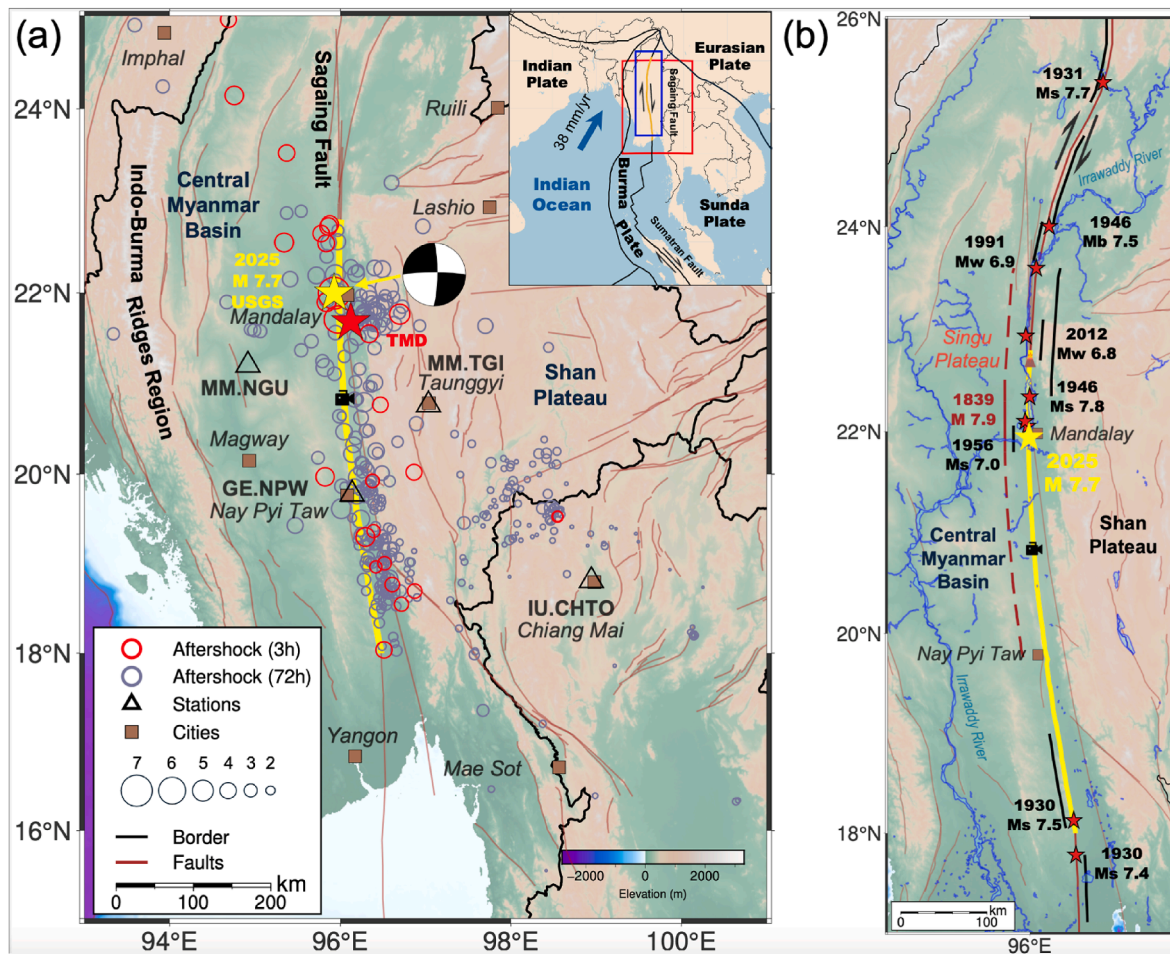


Fig. 1. The 2025 Mw 7.7 earthquake hypocenter near Mandalay, Myanmar, seismic activity following the mainshock and its tectonic setting. (a) Map showing aftershock distribution within 3 and 72 h following the 2025 Mw 7.7 mainshock, along with seismic stations (triangles) and major cities (brown squares). The yellow and red stars mark the mainshock hypocenters from the USGS and TMD catalogs, respectively. The black camera sign shows the location where a surface rupture video was captured by a security camera (e.g., [Latour et al., 2025](#); [Zhang et al., 2025](#); [Hirano et al., 2025](#)). The inset map displays the regional tectonic setting, including the Eurasian, Indian, Burma, and Sunda plates, and other major faults. (b) Historical large earthquakes ($M \geq 6.8$) along the Sagaing Fault. The ~ 500 -km-long rupture zone of the 2025 event is marked as yellow rectangle. Each historical event's rupture length is shown as an orange rectangle. Hypocenter locations and rupture lengths are based on [Xiong et al. \(2017\)](#) and [Hubbard and Bradley \(2025\)](#).

rupture started near the epicenter near 22°N and initially propagated northward over approximately 100 km ([Fig. 2b](#)). It then progressed southward, releasing most high-frequency energy in that direction. The southward rupture extended for at least 300 km, and the total rupture duration was approximately 70–90 s, with minor variations among arrays. This relatively long rupture extent significantly exceeds the empirical expectation of no more than 250 km for a Mw7.7 event ([Wells and Coppersmith, 1994](#); [Bradley and Hubbard, 2025b](#)). Although the average rupture velocity is approximately 3–4 km/s, [Fig. 2b–d](#) clearly shows that portions of the southern segments with an average rupture speed of 4.5 km/s. These preliminary findings are generally consistent with the sub-event and finite-fault inversion analysis ([Bradley and Hubbard, 2025b](#); [Goldberg et al., 2025](#); [Inoue et al., 2025](#); [Antoine et al., 2025](#); [Ye et al., 2025](#)) and other back-projection results ([Antoine et al., 2025](#); [Vera et al., 2025](#); [Wei et al., 2025](#); [Xu et al., 2025b](#)). Together, these studies provide strong evidence for the occurrence of southward-propagating supershear rupture. This observation is also consistent with previous studies suggesting that supershear rupture is commonly associated with strike-slip earthquakes ([Wang et al., 2016b](#)).

4. Early aftershock distributions

Next, we constrain the mainshock rupture length from the locations of early aftershocks following the M7.7 mainshock. Aftershock rates

typically decay with time since the mainshock following the Omori's law ([Utsu et al., 1995](#)), while the aftershock area expand from the mainshock rupture region, generally following logarithmic time since the mainshock ([Peng and Zhao, 2009](#)). Hence, the best time to use aftershock location to reflect the mainshock rupture area would be immediately following the mainshock (i.e., hours to one day) ([Henry and Das, 2001](#)). However, global seismic catalogs such as the USGS or the Global Centroid Moment Tensor (CMT) catalogs typically have a relatively high magnitude of completeness (M_c) of about 5, especially right after the mainshock ([Iwata, 2008](#)). Hence, the numbers of early aftershocks from global catalogs are typically not enough to provide a reliable constraint on the mainshock rupture area. On the other hand, regional earthquake catalogs contain more smaller events that can be used to delineate the aftershock zone and the mainshock rupture area ([Lengine et al., 2012](#); [Bradley and Hubbard, 2025a](#)).

We collect regional and global earthquake catalogs for this region since March 2025 and merge them into one uniform catalog ([Table S1](#)). Among them, the Thai Meteorological Department (TMD) earthquake catalog contains the greatest number of events and is used primarily for the rest of the analysis. Because the Thailand catalog is built from seismic stations primarily in Thailand, their location uncertainties are relatively high. Hence, we select earthquakes within 50 km of the N-S striking Sagaing Fault (centered at the mainshock location as determined by the USGS). The lower-magnitude cut-off decays with time

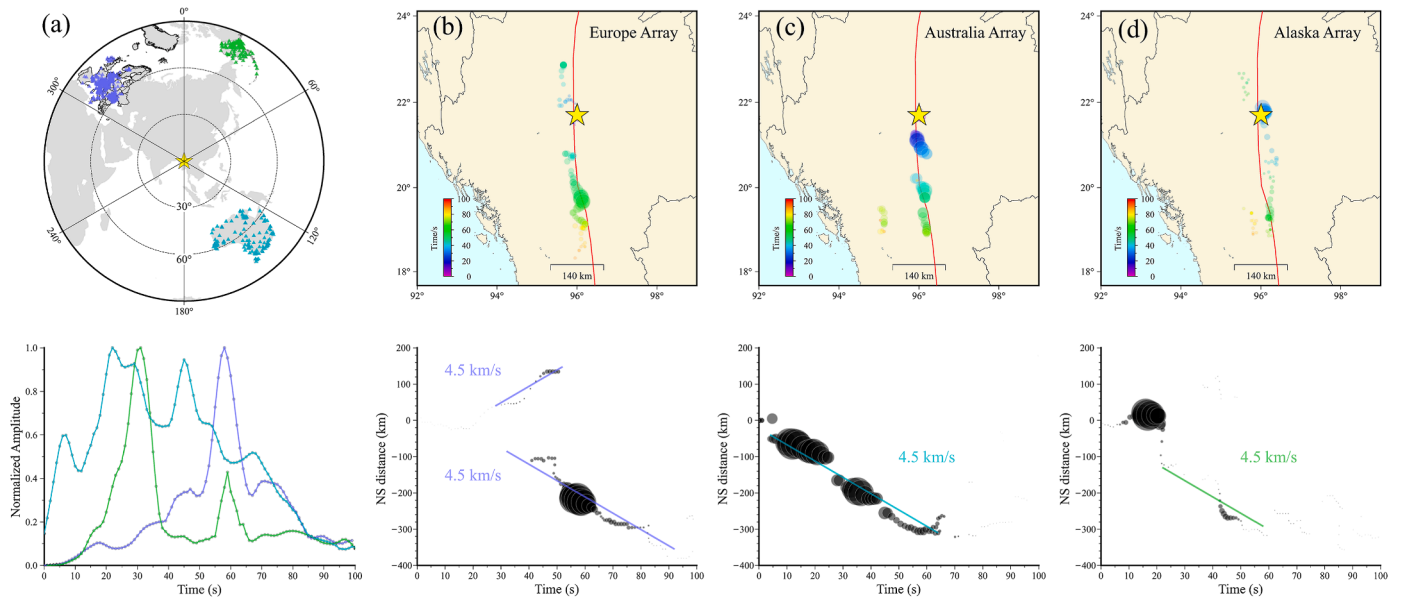


Fig. 2. Teleseismic P-wave back-projection of the 2025 Sagaing Fault earthquake. (a) (Top) Locations of the Europe (EU), Australia (AU) and Alaska (AL) regional seismic arrays. (Bottom) The normalized amplitudes as a function of time for three arrays. (b) Top: spatial distribution, timing, and amplitude of maximum-correlation back-projection beams at 1-s intervals using the Europe array for the 2025 Sagaing Fault earthquake. Bottom: time–distance plot showing the rupture propagation speed of the maximum energy point over time. The yellow star indicates the mainshock epicenter. (c) and (d) Same as (b), but using the Australia and Alaska arrays, respectively.

since the mainshock (Fig. 3a), reflecting that a significant fraction of aftershocks is not detected right following the mainshock (Kagan, 2004). Within the first 3 h following the mainshock, we find 17 aftershocks along the N-S striking Sagaing Fault, which clearly define a ~500-km-long zone that can be interpreted as the mainshock rupture zone (Fig. 3b). We note a relative lack of early aftershocks between 19.5°N and 21.5°N. Although aftershocks occurred slightly later in this region, its density is not smaller than the sections above and below (Fig. 3b).

In addition to directly using the regional TMD catalog, we examine the continuous waveforms for the 4 nearest stations within 500 km of the mainshock epicenter (Fig. 1a). These include two stations in Myanmar’s national seismic network (netcode: MM) (Thiam et al., 2017), one station GE.NPW operated by the GFZ Helmholtz Center for Geosciences (GFZ) (Lai et al., 2025), and one Global Seismic Network (GSN) station IU.CHTO. We apply a band-pass-filter of 5–15 Hz to suppress the coda of the mainshock and large aftershocks, followed by taking a smooth function with a half-width of 100 point and finally

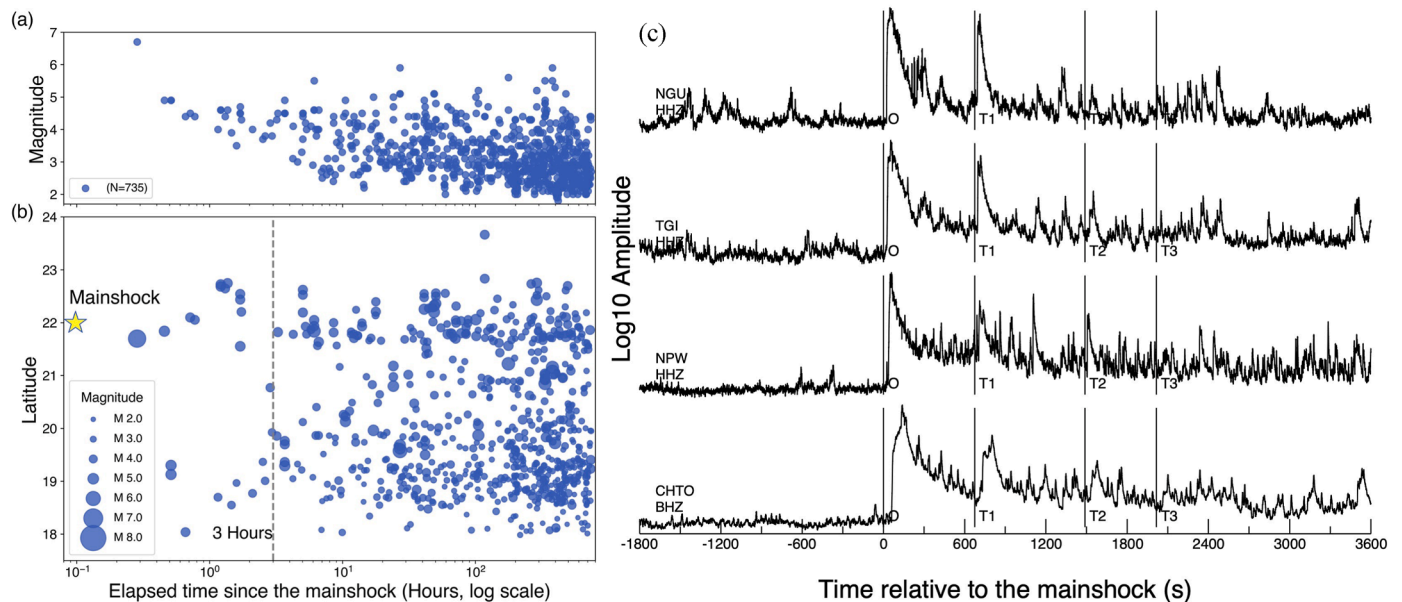


Fig. 3. Aftershock activities from the regional TMD catalog and continuous waveforms. (a) Magnitude versus elapsed time (in hours, log scale), showing temporal evolution of the aftershock. (b) Latitude versus elapsed time (in hours, log scale). Circle sizes are scaled by magnitude, as shown in the legend. A vertical dashed line at 3 h highlights the early aftershock. (c) 5–15 Hz band-pass-filtered envelope functions of waveforms recorded over a 1.5-h period around the M7.7 mainshock by the vertical components of 4 nearest stations. The time flags (0, T1, T2 and T3) mark the origin time of the mainshock, the M6.7 aftershock and two additional aftershocks recorded in the TMD catalog.

taking the log10 (Peng et al., 2006, 2025). In addition to those 4 events (including the M7.7 mainshock) listed in the regional and global catalogs within the first hour of the mainshock, many high-frequency bursts can be visually identified (Fig. 3c). These events either occurred along the Sagaing Fault as early aftershocks, or they may occur off the Sagaing Fault as triggered seismicity.

Beyond the N-S along-strike distribution, aftershocks are scattered in the E-W direction for up to 100 km long (Fig. 1a). In particular, a significant portion of aftershocks near the epicenter (around 22° N) occurred to the east to the Sagaing Fault. In addition, aftershocks south of the epicenter and Naypyidaw (around 20° N) are relatively sparse, which is also shown in the along-strike versus log-time plot since the mainshock plot (Fig. 3b). We then generate a zoom-in plot to show the aftershock distribution on top of pre-existing faults south of the mainshock epicenter (Fig. 4a). Although some aftershocks occurred to the west of the Sagaing Fault in the CMB, majority of them occurred within the Shan Plateau to east of the Sagaing Fault (Fig. 4a and d). We also perform a comparison of the common events listed in the USGS and TMD catalogs (Fig. 4d-g). We note that aftershocks in the TMD catalog were systematically located to the Shan Plateau side, and the mean/median

difference in the fault-normal distance is about 25 km (Fig. 4h). A similar comparison for the 5-yr of seismicity before the mainshock shows similar but smaller mean/median differences between these catalogs (Fig. S1). Hence, at least some of the aftershock shift to the Shan Plateau can be explained by such a bias in the aftershock locations in the TMD catalog, if we assume that the USGS location is the ground truth.

5. Seismicity before the mainshock and mainshock/aftershock waveforms

In this section, we focus on the seismic activity in the last few weeks before the M7.7 mainshock, the first few seconds of the mainshock rupture, and aftershock waveforms. By examining both the regional Thailand earthquake catalog within one year of the mainshock and the continuous waveforms in the last few hours, we find no single event occurring within 50 km of the mainshock epicenter in the last three months (Fig. 3c; Fig. S2). Hence, similar to the 2023 M7.8 Pazarcik event in the Kahramanmaraş, Türkiye, Earthquake Sequence (Kwiatk et al., 2023), no immediate foreshock was identified.

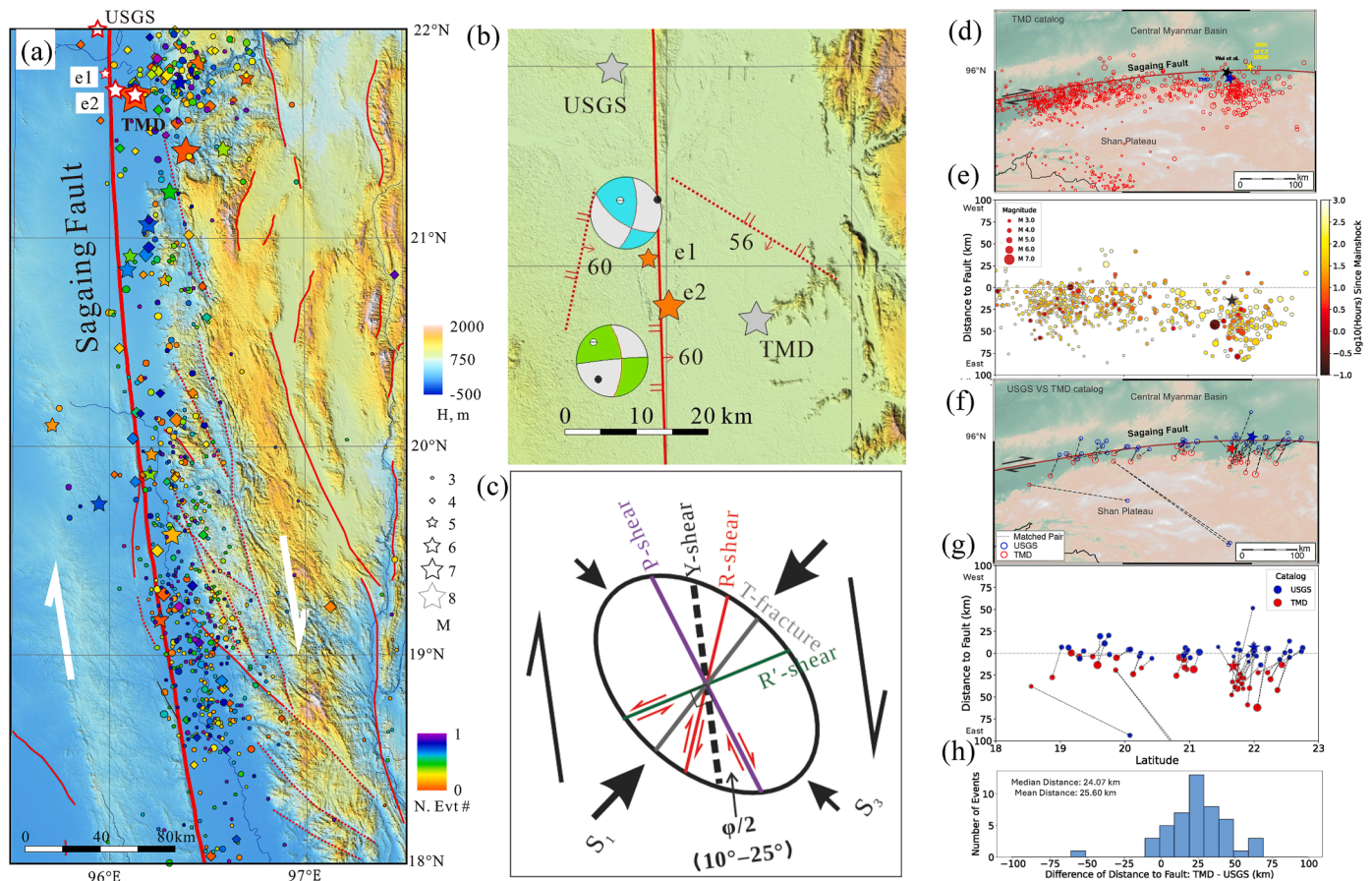


Fig. 4. Spatial distribution and catalog comparison of the 2025 M7.7 mainshock and its aftershock. (a) A zoom-in plot showing aftershock locations listed in the TMD catalog relative to the mainshock rupture trace (thick red line). The thin red solid and dashed lines mark the local fault traces and those visually identified based on geomorphic features. (b) The hypocentral locations and focal mechanisms of the sub-event (e1) and main event (e2) (see text and Fig. 6 for details), as compared with the mainshock locations listed in the USGS and TMD catalogs. (c) The distributions of different types of shears and fractures under the current maximum horizontal stress directions. (d) Epicentral distribution of the TMD catalog, with events sized by magnitude. The Sagaing Fault trace and regional tectonic features such as the Central Myanmar Basin and Shan Plateau are annotated. The yellow star marks the USGS mainshock location, the black star shows the location from Wei et al. (2025), and the blue star indicates the TMD mainshock location. (e) Distance of aftershocks to the Sagaing Fault as a function of latitude, where the vertical axis represents the perpendicular distance mapped onto the fault trace. The spatial distribution of seismicity across the fault is evident, with temporal evolution illustrated by the color scale (logarithmic hours since the mainshock). (f) Comparison of matched events between the USGS (blue) and TMD (red) catalogs, plotted by latitude (horizontal axis) and longitude (vertical axis). Dashed lines connect each matched pair, illustrating differences in their locations and their respective distances to the Sagaing Fault. (g) Distance-to-fault values plotted against latitudes for all matched events. USGS (blue) and TMD (red) locations are shown for each pair, with vertical dashed lines connecting the corresponding points. (h) Histogram of differences in fault-perpendicular distance between matched TMD and USGS events. The median and mean offsets are calculated as the distance from each TMD event to the fault minus that of its USGS counterpart.

A close examination of the mainshock waveforms at the nearest three stations reveal additional details on the initial and mainshock rupture phases (Fig. 5a). Here we do not apply any filters or instrument corrections to the broadband recordings but only plot them in different amplitude and time scales. We also include the velocity seismogram integrated from the acceleration recordings (HN channels) at station GE.NPW that is about 2.6 km west of the M7.7 mainshock surface rupture zone (Lai et al., 2025). While it is still possible to identify the initial S waves at stations MM.NGU and MM.TGI before the broadband recordings went off-scale, the broadband recordings at station GE.NPW went off-scale much earlier than the predicted S arrivals (Fig. 5a). However, the on-scale velocity seismograms from integrating the acceleration shows a strong pulse arriving at 48.5 and 51 s, with the peak value of 1.64 m/s at ~ 50 s. Here we use the reference origin time of 2025/03/28 06:20:55.209 UTC (Wei et al., 2025). If we also use their mainshock location (21.641°N, 96.022°E, 10 km depth), the corresponding hypocentral distance and rupture speed would be 206.6 km and 4.13 km/s, respectively. This observation again confirm that the southward rupture propagation is primarily supershear (Lai et al., 2025; Wei et al., 2025; Xu et al., 2025a, 2025b, 2025c; Goldberg et al., 2025; Inoue et al., 2025).

Fig. 5 also shows the zoom-in plots of the P waves at three stations, including a comparison with the P wave at the same GE.NPW station for a M4.6 aftershock on 2025-04-04 15:25:24 UTC (10 km depth, 21.5621°N). A strong phase in the same direction is shown at stations MM.NGU, MM.TGI and GE.NPW after ~ 3.7 , ~ 3.6 and ~ 2.5 s of the initial P waves, respectively. Because of the increasing distances from the initial hypocenter to these stations, we expect to see an increasing time separation of we interpret these phases as the Pn and Pg waves. Hence, we argue that the second strong phase (e2) is likely from a second stronger sub-event following the initial P wave of the first event (e1). Because of the shorter time separation at station GE.NPW, we expect that the second source is closer to this station, indicating a southward propagation of the rupture. Note that station GE.NPW has about 0.78 s of

timing drift at the time of the mainshock (Lai et al., 2025). However, here we use only the relative time difference between these phases and hence it is not affected by such a timing issue.

To better locate these sub-events, we collect additional waveform data from the Yunnan Network in Southwest China, manually pick the first arrivals of the first sub-event (e1), and relocated it using the western Yunnan average velocity model (Table S2) (Yao, 2020). The relocated initial hypocenter coordinates are 21.759°N, 95.975°E at a depth of 18.7 km, with an estimated magnitude of $\sim M6$. The corresponding origin time is 2025/03/28 06:20:52 UTC (Table S3). The mainshock (e2) occurring ~ 3 s later, is located 21.699°N, 96.003°E at a depth of 24.8 km at 6 km southeast of e1 (Table S3, Fig. 6). Both events lie intermediate between the initial hypocenters from the USGS and TMD catalogs, while their depths are near the lower boundary of the coseismic rupture distribution inverted from InSAR and other geodetic/seismic datasets (Antoine et al., 2025; Wei et al., 2025; Goldberg et al., 2025; Ye et al., 2025), suggesting potentially higher accuracy.

We further refine the USGS CMT solution using P-wave first-motion polarities, finding that modifying the fault dip to 60° is necessary to satisfy all clear first-motion observations (Fig. 6b). After multiple parameter adjustments, the optimal focal mechanism for e1 was determined as Strike = 10° , Dip = 60° , Rake = 140° (Fig. 6a). This solution reconciles the observed opposite P-wave first-motion polarities between e1 and e2 at selected stations.

We note that the initial polarity of the M7.7 mainshock at station GE.NPW is down, while the initial polarity of the M4.6 aftershock is up (Fig. 5). The expected polarity for a right-lateral strike-slip event at station GE.NPW is down for a homogenous medium. However, most of the aftershocks north of this station shows a weak upward motion followed by a strong downward motion (Fig. 7). The initial phases from selected $M > 4$ aftershocks can be interpreted as fault zone head waves (FZHWs) refracted along a bimaterial fault interface (Ben-Zion and Malin, 1991; Zhao and Peng, 2008; Zhao et al., 2010; Allam et al., 2014), which would be recorded as the first arrivals for stations on the slower

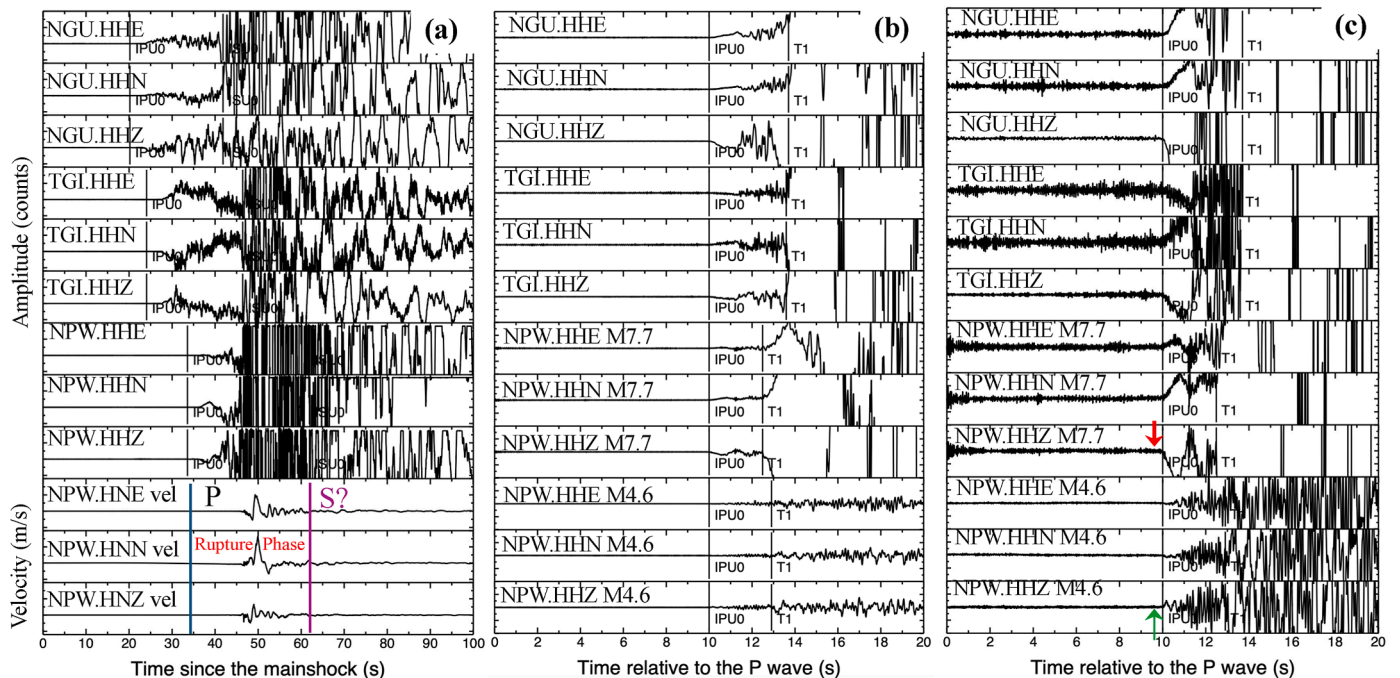


Fig. 5. (a) A comparison of the first 100 s of the M7.7 mainshock recording at the three broadband stations. The bottom three traces are velocity seismogram integrated from the strong-motion recordings at station GE.NPW ~ 2.6 km west of the mainshock rupture zone. The P and S lines mark the expected P and S arrivals at this station. (b) A Zoom-in plot showing a comparison between the P waves of the M7.7 mainshock with respect to a M4.6 aftershock close to the relocated mainshock hypocenter on 2025/04/04. (c) A further zoom-in plot showing the initial P wave polarity. Note that the polarity of the M7.7 mainshock and the M4.6 aftershock at station GE.NPW is flipped.

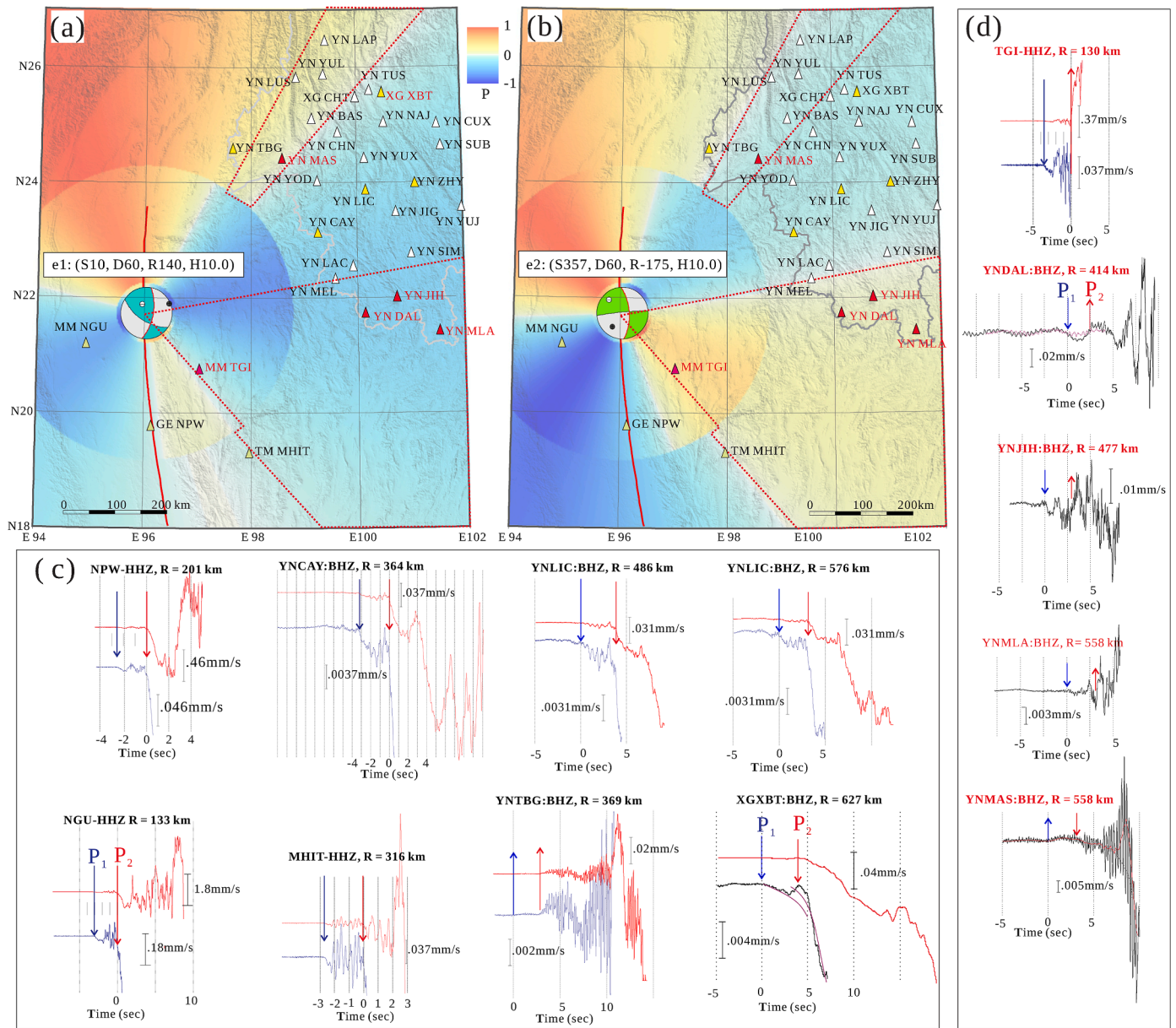


Fig. 6. Maps showing the suggested focal mechanism of the sub-event e1 (a) and the modified CMT solution of the mainshock e2 (b) with P radiation patterns and seismic stations. Regions outlined by dot lines show opposite P-wave first-motion polarities between e1 and e2. (c/d) Waveforms at selected stations in regions where e1 and e2 have consistent/opposite P-wave first-motion polarities.

side of the fault (i.e., the Central Myanmar Basin in this case). By fitting the time delays between the initial FZHWs and direct P waves, we obtain an average velocity contrast of 5–7 % (with an assumed average P wave velocity of 5.5 km/s).

6. Tidal triggering of the mainshock?

In this section we evaluate whether solid Earth tides have played any role in the eventual timing of the mainshock, which has been a subject of debates for decades (Ide et al., 2016; Hough, 2018; Bradley and Hubbard, 2024). We calculate the strain tensors generated by solid Earth tides and ocean tides using the program GOTIC2 (Matsumoto et al., 2001), which employs the 1066A elastic Earth model (Dziewonski et al., 1975). To enhance the accuracy of ocean tidal loading effects, GOTIC2 incorporates the improved ocean tide model NA0.99b, which was widely used in previous studies on tidal triggering of earthquakes (Tanaka, 2012). The computed strain is then converted to stress using a

bulk modulus of ~42 GPa and a shear modulus of ~28 GPa, derived from the average P-wave and S-wave velocities and density in the 3–15 km depth range of the 1066A model. Tidal strains are independent of fault orientation. However, for faults with specified strike, dip, rake, and frictional coefficient, we further calculate the normal stress, shear stress, and Coulomb Failure Stress (CFS) to evaluate tidal response.

Since the mainshock occurred just before the new moon (03/29/2025), we first calculate the tidal strains and stresses from long-period waves on a fault with orientation (strike, dip, rake) = (358°, 82°, -175°), corresponding to the USGS CMT solution. The mainshock timing coincides with peaks in volumetric strain, and CFS (Fig. 8a). Notably, the amplitudes of long-period waves modulate those of diurnal and semi-diurnal tidal waves. We further computed tidal stresses for all tidal components (long-period, diurnal, and semi-diurnal) over time spans of 10 days. The results reveal that both the mainshock and some large aftershocks ($M \geq 5.0$) coincide with peaks in CFS or shear stress (Fig. 8b). Although this correspondence between the timing of

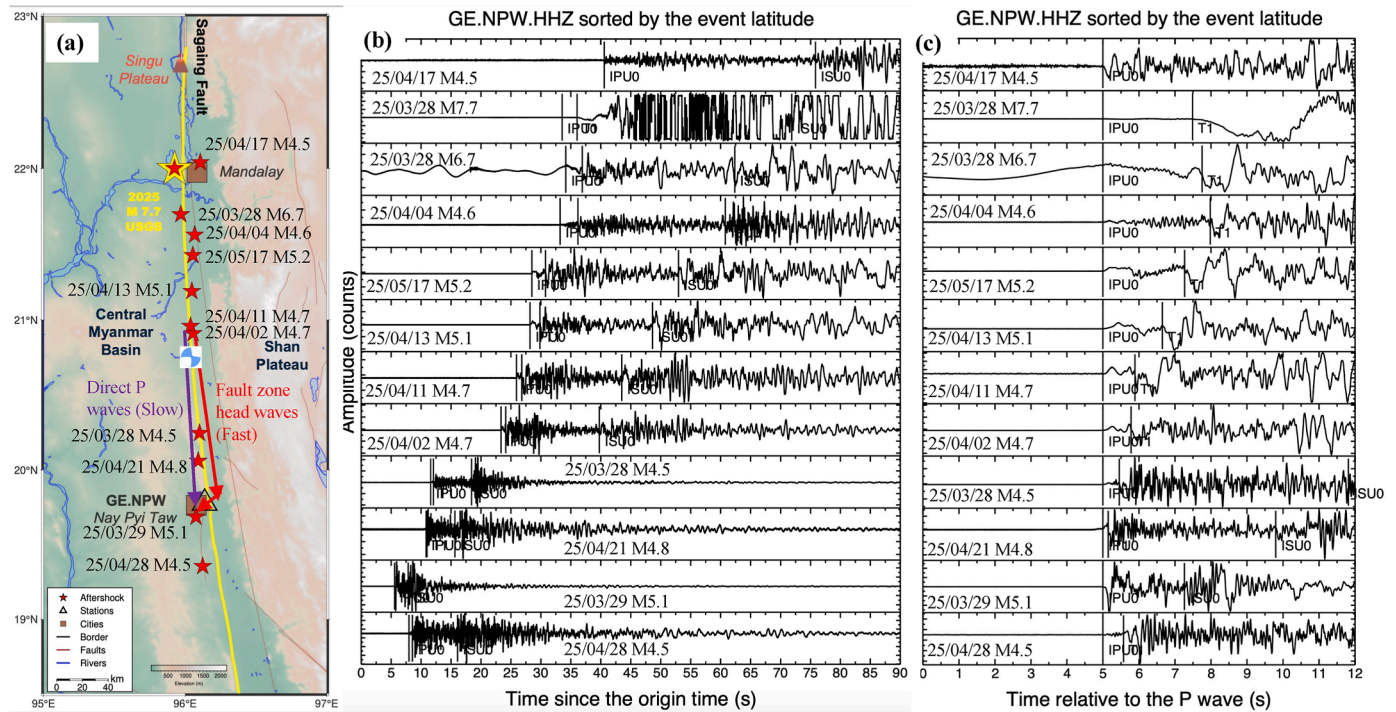


Fig. 7. (a) A map showing the locations of the M7.7 mainshock and other 11 aftershocks. The red and purple arrows mark the expected ray paths for fault zone head waves along the faster side (Shan Plateau), and the direct P wave along the slower side (Central Myanmar Basin). (b) Vertical-component seismograms recorded at station GE.NPW sorted by the event latitudes. The initial weak P waves, abrupt secondary arrivals, and the S waves are marked. (c) Same plot as (b) except that all traces are aligned by the initial P waves.

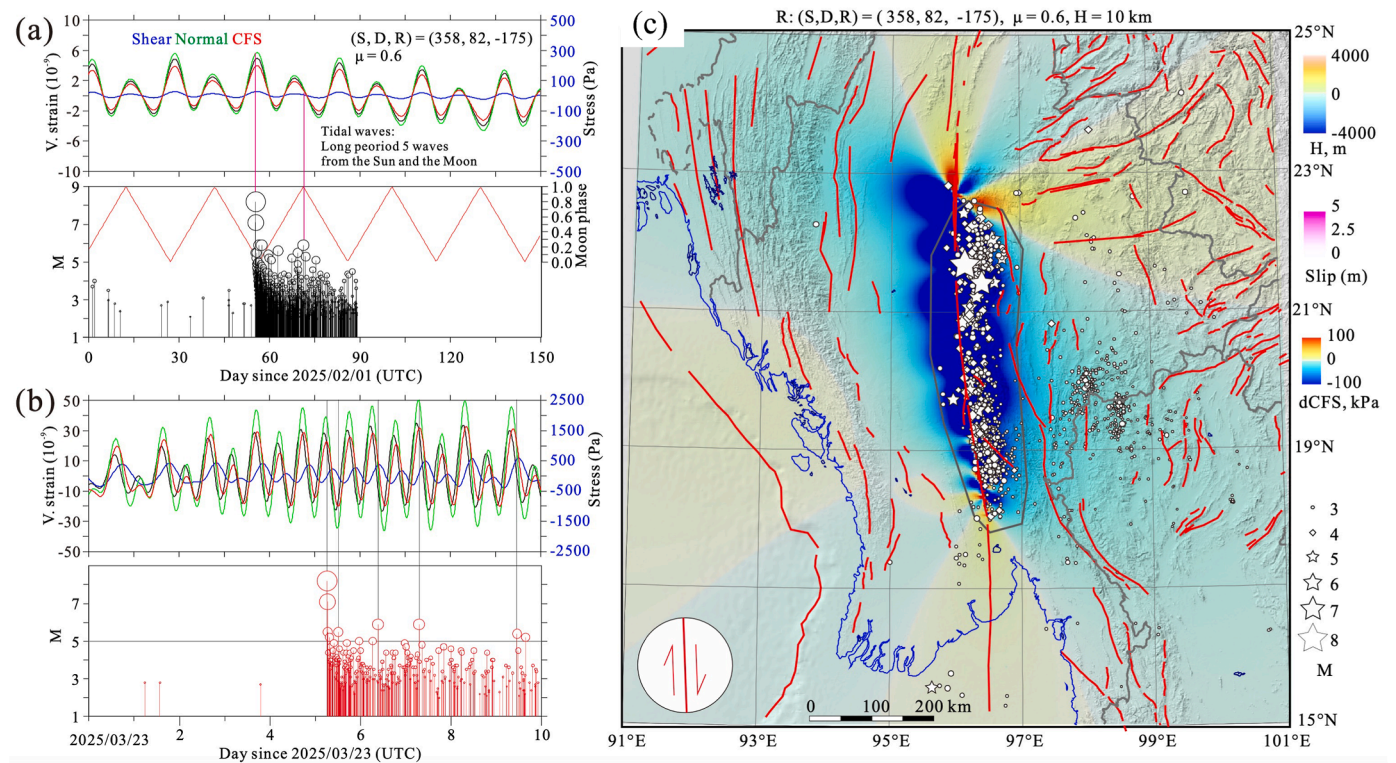


Fig. 8. Comparison of tidal strains/stresses and earthquake occurrence times. (a) Long-period tidal wave components and M-T plot. (b) Full tidal wave spectrum (including diurnal, semi-diurnal, and long-period components) and M-T plot for 10 days since March 23, 2025. (c) Map view of active faults and earthquake distribution overlying on change of Coulomb Failure Stress (Δ CFS) from the 2025 M7.7 mainshock for faults parallel with the Sagaing Fault; events within the outlined polygon are analyzed in panels (a)–(b).

earthquake occurrence and peak tidal stress may largely be attributable to statistical contingency in the absence of a more robust chain of evidence, documenting the fact itself holds certain significance. It adds a potential instance supporting the inference that “large earthquakes are more probable during periods of high tidal stress” (Ide et al., 2016).

7. Coulomb stress changes from the mainshock

Large earthquakes are expected to transfer static stresses to nearby faults and change the occurrence of future earthquakes on those faults (Stein, 1999). Several recent studies have examined how previous earthquakes loaded the central and southern section of the Sagaing Fault before the M7.7 mainshock (Xiong et al., 2017). In addition, rapid analyses also revealed how static Coulomb stress changes Δ CFS from the 2025 M7.7 mainshock would affect earthquake occurrences on faults parallel to the Sagaing Fault (Toda and Stein, 2025) and other faults in the neighboring Yunnan province in Southeast China (Li et al., 2025). Here we adapt the coseismic fault slip model published by the USGS and the crustal model for tidal stress calculation to compute the coseismic static stress changes of the M7.7 mainshock on surrounding areas. For comparison, we first calculate the Coulomb stress changes on receiver faults parallel to the Sagaing Fault. The results are shown in Fig. 8c with superimposed aftershock distributions from the TMD catalog. As expected (Stein, 1999), numerous aftershocks with the same receiver fault as the mainshock rupture segment are distributed within stress shadow zones. Fig. S3 shows a similar calculation but for receiver faults that are nearly E-W trending. Those faults are distributed mainly along the Myanmar-China border (Li et al., 2025). The M7.7 mainshock rupture casted a positive stress changes (on the order of a few to a few tens of Kpas) to those faults north of 21°N. Further to the south, most of the E-W trending faults would be in the stress shadow, similar to the other two receiver fault geometries (Fig. 8c and 9a).

As noted before, most aftershocks occurred in the eastern side of the Sagaing Fault, which features a relatively complex secondary fault network, and appears to dominantly control aftershock occurrence. Analysis of aftershock clustering characteristics and known fault

geometries suggests that faults striking N30°W with a dip angle of 45° (Fig. 4) may constitute one of the seismogenic structures for these aftershocks, with corresponding Coulomb stress changes illustrated in Fig. 9a. Due to fault bend and heterogeneous coseismic slip, some stress-enhanced areas emerge in both sides of Sagaing Fault zone. Given the substantial uncertainties remaining in the mainshock fault model and hypocenter locations, we conclude that the eastern side of the Sagaing Fault possesses a more complex secondary fault network than the western block, which hosts most aftershock activity. Fig. 9b also shows for receiver faults striking E30°W with a dip angle of 56°, same to the conjugate fault of the source fault suggested for e1 shown in Fig. 4a. Interestingly, most aftershocks fall in regions of positive Coulomb stress changes Δ CFS. These faults likely represent relatively optimal oriented potential sub faults surrounding the Sagaing Fault, especially at its east side in the Shan Plateau. These calculations highlight the importance of receiver fault geometry on the resulting signs of the Δ CFS and aftershock triggering mechanism.

8. Remotely triggered seismicity in Southeast Asia

Large strike-slip earthquakes can generate strong surface waves (especially Love waves) that are capable of triggering both regular microearthquakes and deep tectonic tremor at thousands of kilometers (Prejean et al., 2004; Peng and Chao, 2008; Peng and Gomberg, 2010; Pollitz et al., 2012; Hill and Prejean, 2015; Yao et al., 2024). Hence, we expect that the M7.7 mainshock are also capable of triggering seismic activity well beyond the traditional aftershock zone, also known as remotely triggered seismicity. Here we focus on the following three regions (Southeast of Myanmar, Yunnan province in Southeast China and Guangdong province in South China), mainly because of easy access of both regional catalogs and waveform data.

In the southeast of Myanmar lies the Shan Plateau, a topographic high with an average elevation of about 1000 m that extends from Thailand to the Yunnan province, China (Bertrand and Rangin, 2003). Many earthquakes with moment magnitudes larger than 6 have occurred in the past century (Wang et al., 2014), especially the 1912 Ms

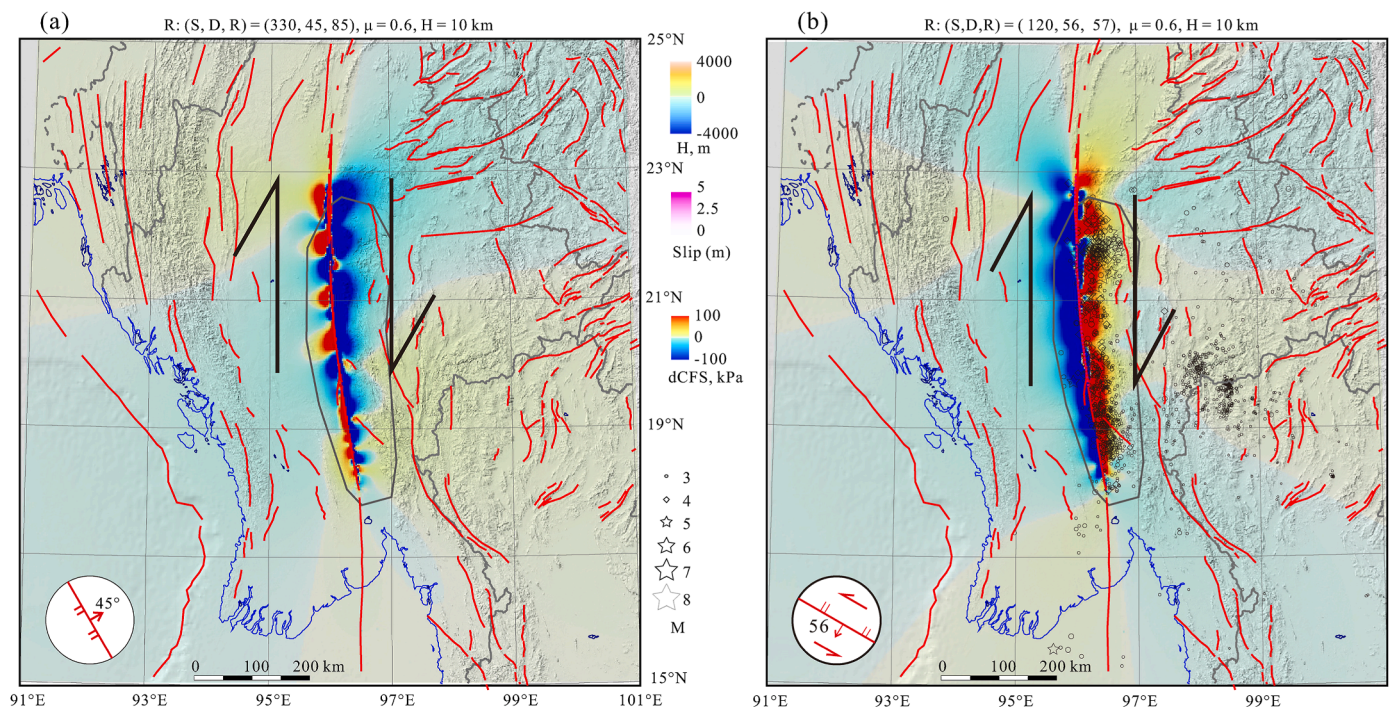


Fig. 9. (a) Map view of active faults and earthquake distribution overlying on change of Coulomb Failure Stress (Δ CFS) from the 2025 M7.7 mainshock for receiver fault of (strike, dip, rake) = (330, 45, 85), frictional coefficient of 0.6, and at a depth of 10 km. (b) The same plot for receiver fault of (strike, dip, rake) = (120, 56, 57), frictional coefficient of 0.6, and at a depth of 10 km.

7.7 Maymyo earthquake near the Taunggyi city (Crosetto et al., 2019). The recorded events in this region are mainly located near the Kyaukkyan fault, which extends southward to the Mae Ping fault zone running along the Myanmar-Thailand border (Wang et al., 2014). While this region is not well studied in terms of remote dynamic triggering, a Mw 5.8 earthquake near Namzang, Myanmar, occurred 30 min following the 2004 M9.1 Sumatra earthquake, with another Mw 5.1 event happening 4 days after (Ruan, 2007), indicating that this region is susceptible to remote dynamic triggering (Fig. 10a). Another group of earthquakes is in northern Thailand, close to the Myanmar border. This region is filled with faults running across major provinces in northern Thailand, including Mae Hong Son and Chiang Mai. Events in this area are mainly associated with the Mae Hong Son fault and the Mae Tha fault, respectively. A Mw 5.6 earthquake in February 1975 likely ruptured near the southern part of the Mae Hong Son fault (Chansom et al., 2022).

Since several of the Myanmar National Seismic Network's broadband stations (Thiam et al., 2017) are currently inactive, the detection of events in this region largely depends on the seismic stations operated by the TMD, which are deployed in the northern and northwestern parts of Thailand. Fig. 10a shows the spatial distribution of events in this study region 30 days before and after the 2025 M7.7 earthquake. A significant increase in the cumulative number of events is observed after the mainshock (Fig. 10c). This suggests that the earthquakes in this specific area of Myanmar and Thailand were remotely triggered immediately by the Mw 7.7 mainshock. Coulomb stress calculations from the previous section (Fig. 8c and 9) indicated that static stress changes from the mainshock are negative and on the order of ~ 1 Kpa or less in this region. Fig. 10b shows first 6000 s after the mainshock at the seismic station TM.CMMT in Chiang Mai, Thailand, recording the Mw7.7 mainshock, the largest aftershock of Mw6.7, multiple aftershocks, and a local triggered event Ms3.3 in Mae Hong Son, Thailand. Many high-frequency signals are recorded immediately following the mainshock that were not listed in the TMD catalog. They are likely local seismicity in that region triggered by the M7.7 mainshock. Because of the aforementioned negative

static stress changes (i.e., stress shadow), the observed sudden increase of seismicity in the Shan plateau can be best explained as triggered by dynamic stress changes from the passing waves of the M7.7 mainshock. This is consistent with the previous observation of remote dynamic triggering in this region following the 2004 M9.1 Sumatra earthquake (Ruan, 2007).

Yunnan Province, situated on the southeastern margin of the Tibetan Plateau, is a tectonically complex and seismically active region influenced by the ongoing convergence between the Indian and Eurasian plates. Major fault zones in this area including the Red River Fault Zone (RRFZ), Xiaojiang Fault, and Nujiang Fault, which have hosted frequent moderate-to-strong earthquakes. In addition, previous studies have shown that several faults in Yunnan, including the Tengcong volcanic regions, are prone to dynamic triggering by teleseismic waves from large distant earthquakes (Lei et al., 2011; Li et al., 2019). The triggered seismicity mostly occurred in sites with complex fault geometries or volcanic/geothermal areas, likely due to the presence of high-fluid pressures in these regions (Hill and Prejean, 2015).

After the 2025 Mw 7.7 Myanmar mainshock, enhanced seismicity was observed in western and southern Yunnan. Post-mainshock earthquakes (red circles) cluster around the RRFZ and nearby fault systems (Fig. 11a). Notably, Fig. 11b highlights a group of events that occurred nearly simultaneously with the arrival of the surface waves from the mainshock, strongly suggesting dynamic triggering. This spatiotemporal pattern aligns with observations from previous events such as the 2004 Sumatra and 2012 Indian Ocean earthquakes, which also remotely triggered seismicity in Yunnan (Lei et al., 2011; Li et al., 2019). These results further confirm that faults in Yunnan remain highly responsive to dynamic stress perturbations and represent an important natural laboratory for studying remote triggering mechanisms.

The Xinfengjiang Reservoir in the Guangdong province in South China represents one of only four documented cases globally where reservoir has occurred $M \geq 6$ seismic events (Foulger et al., 2018). Following the 1962 M6.1 mainshock, persistent low-magnitude seismic activity ($ML < 3$) has been systematically recorded in this region. The

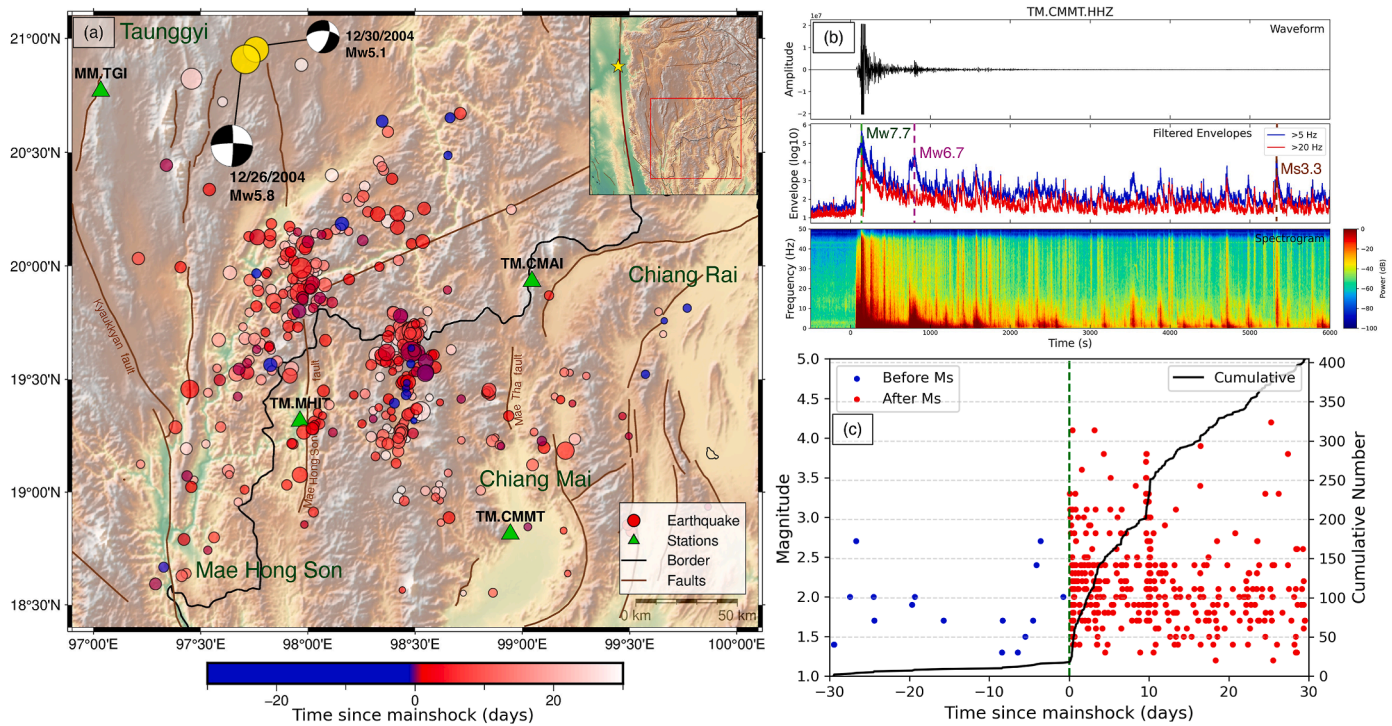


Fig. 10. (a) Spatial distribution of earthquakes 10 days before and after the Myanmar earthquake on March 28th, 2025. (b) The \log_{10} envelope function of the vertical component, 5000 s after the mainshock, recorded at three broadband stations in Thailand. (c) Earthquake magnitude - time plot for the analyzed region, 10 days before and after the mainshock, with the cumulative number of events calculated.

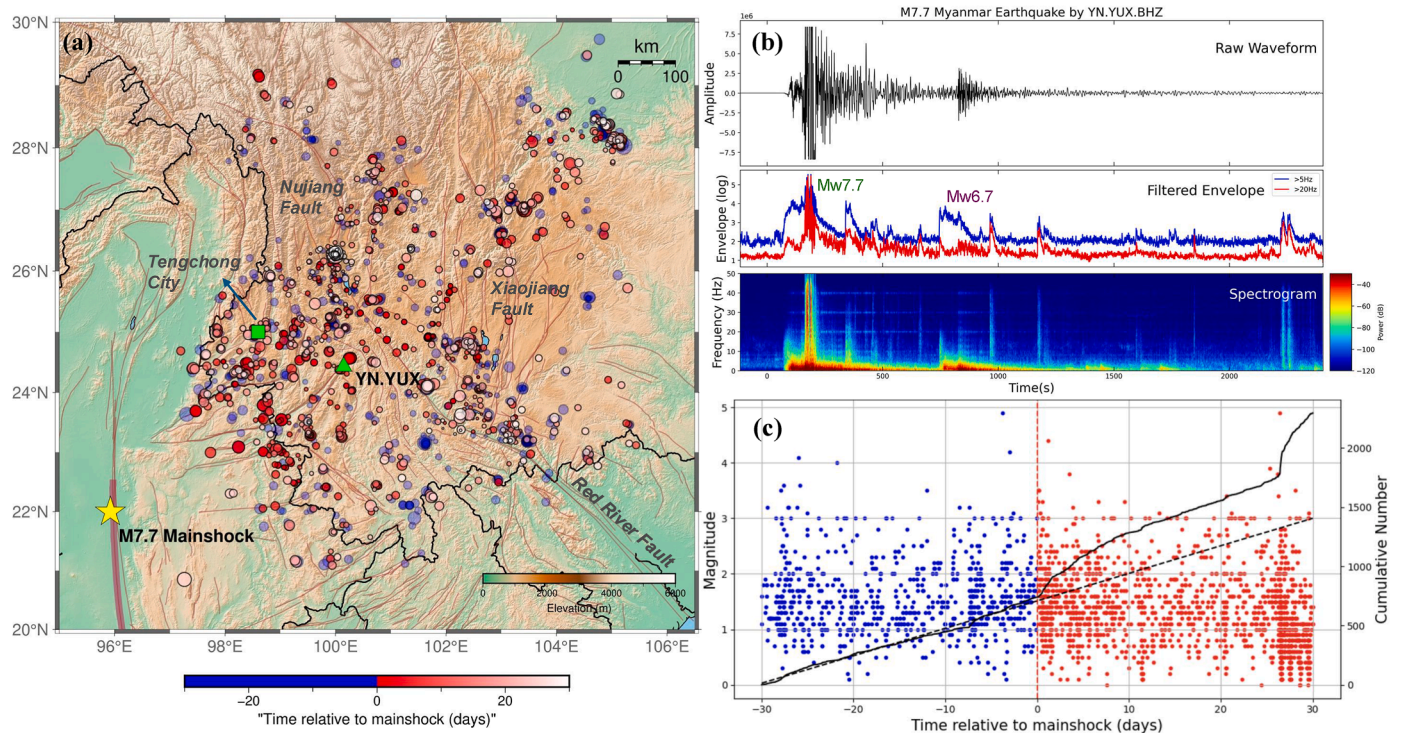


Fig. 11. (a) Spatial distribution of earthquakes within 30 days before and after the 2025 Mw 7.7 Myanmar mainshock (yellow star), with event colors indicating the time relative to the mainshock (blue for before, red for after). Station locations are marked with red triangles, and sparse station names are labeled using network and station codes for clarity. (b) Seismic waveform recorded at station YN.YUX on the vertical (BHZ) component. From top to bottom: the raw waveform, log-scaled high-frequency envelopes filtered at 5 (blue) and 20 (red) Hz, and the corresponding spectrogram. The Mw 7.7 mainshock and the Mw 6.7 aftershock are highlighted in the envelope panel. (c) Time–magnitude plot of earthquakes relative to the mainshock, with blue and red dots representing events occurring before and after the mainshock, respectively. The black curve shows the cumulative number of events during the 60-day window. The dashed line marks the expected number based on the seismicity before the mainshock.

physical mechanisms driving this sustained seismicity remain unresolved (Huang et al., 2025). To enhance seismic monitoring capabilities, the Guangdong Earthquake Agency has established a comprehensive broadband seismic network encompassing the reservoir area. Based on these data, our analysis reveals a notable seismicity pattern associated with the 2025 M 7.7 earthquake. Prior to this teleseismic event, seismic activity in the eastern reservoir (marked by the red rectangle in Fig. 12) remained exceptionally low (5 detectable events) during the last 1 years. Remarkably, within one week following the mainshock, this area experienced a four-times increase in seismicity (>35 events, local magnitude M_L -0.8 to 1.3). This abrupt activation, exhibiting temporal correlation with distant seismic waves and characteristic magnitude distribution patterns, strongly suggests dynamic stress triggering mechanisms. We find no additional evidence of dynamic triggering in other region within the Guangdong province.

9. Discussion

In this study, we perform a detailed analysis of the mainshock rupture properties, initial rupture phases, tidal stress modulations of the mainshock timing, Coulomb stress changes from the mainshock and aftershocks, and remotely triggered seismicity following the M7.7 mainshock. While many of the analysis can be considered as preliminary, we can make several interesting conclusions. First, the mainshock rupture length of up to 500 km can be rapidly determined both from the back-projection of the teleseismic P waves, and early aftershock locations within a few hours following the mainshock (Figs. 2 and 3). Subsequent analysis based on finite-fault inversions, as well as space geodesy observations further confirmed this ultra-long rupture (Antoine et al., 2025; Bradley and Hubbard, 2025; Wei et al., 2025; Xu et al., 2025a, 2025b, 2025c; Goldberg et al., 2025; Melgar et al., 2025; Vera

et al., 2025; Inoue et al., 2025). However, these analyses typically took a few days/weeks to complete and hence would not be applicable immediately following the mainshock. Fig. 3c also shows that many more early aftershocks were recorded by stations at regional distances, but were not detected/located yet, likely due to their overlapping arrivals. Applying advanced earthquake detection/association methods such as template matching, source scanning or machine learning can help to rapidly determine the spread of the aftershock zone (Peng and Zhao, 2009; Liao et al., 2012; Yu and Wang, 2022). Combining with teleseismic back-projection of mainshock ruptures (Wang et al., 2016a; Wei et al., 2025), these approaches can help to define the full extent of the mainshock rupture zone within hours, which are essential for rapid source characterization and subsequent aftershock forecasting.

A rupture length of ~500 km for this event (Fig. 13a) would be comparable to the 1906 M7.9 San Francisco earthquake, which ruptured along the San Andreas Fault in northern California for about 480 km (Song et al., 2008). However, such a long rupture length is somewhat expected for large continental strike-slip faults, which tends to have rupture length/width ratio of 20–30 (Weng and Ampuero, 2019). Recent examples include the 2001 M7.9 Kokoxili earthquake in Central Tibetan Plateau (~390 km long), and the 2002 M7.9 Denali Fault earthquake in Alaska (~340 km) (Ozacar and Beck, 2004). These events likely represent the runaway unstable ruptures (Xu et al., 2015) that can only be stopped by geometric complexities or barrier (Wesnousky, 2006).

Perhaps the most striking feature of this event is its apparent simple mainshock rupture properties (Fig. 13a). Unlike the 2023 M7.8 Pazarcik event in the Kahramanmaraş Earthquake Sequence in Southeastern Türkiye (Fig. 13b), which started on a subsidiary Narli fault before jumping on the main East Anatolian Fault (Xu et al., 2023; Stein and Bird, 2024), the M7.7 earthquake nucleated on or near the north-south striking Sagaing Fault (Goldberg et al., 2025). However, a

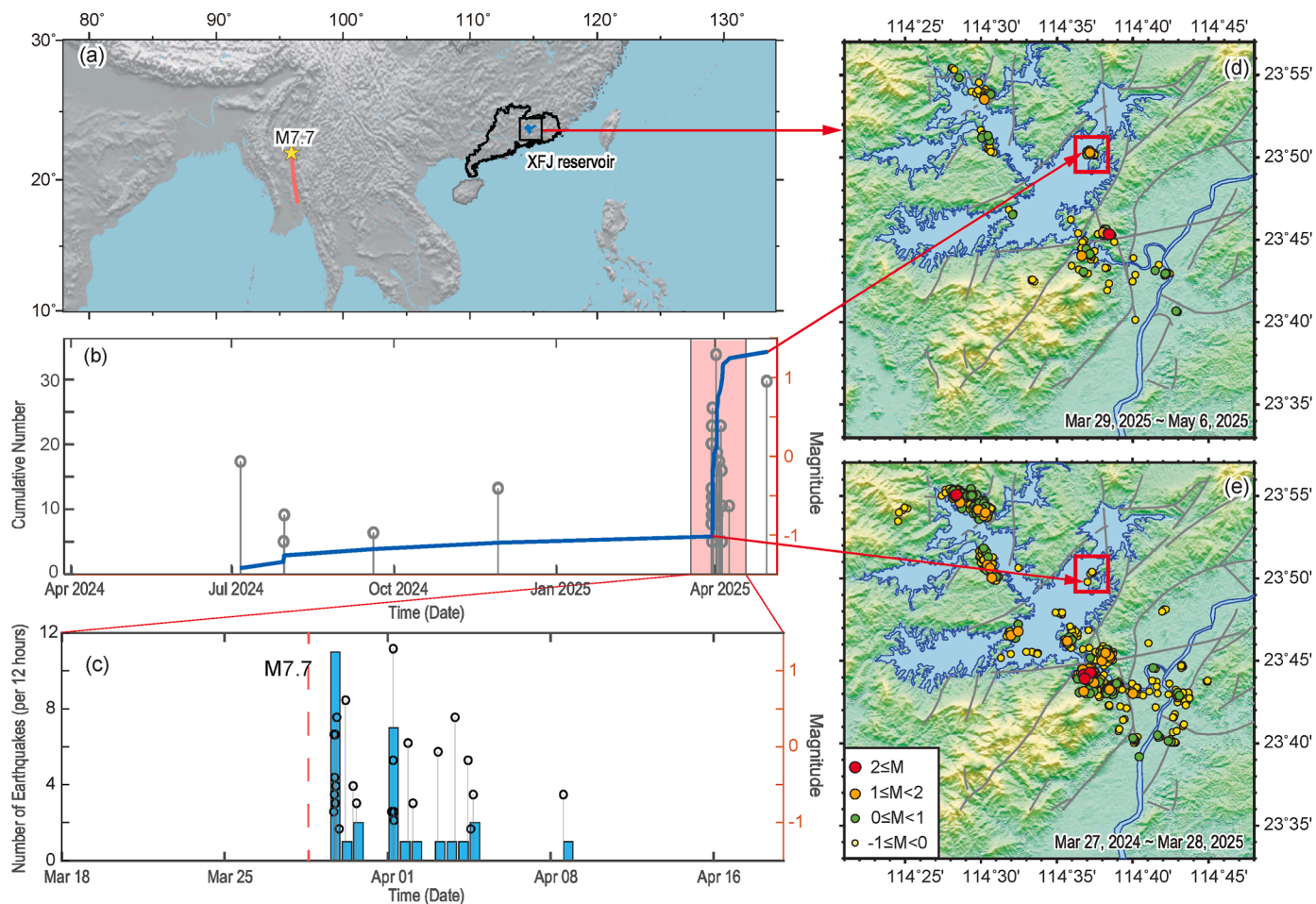


Fig. 12. (a) Locations of the M7.7 mainshock and Xinfengjiang Reservoir. (b) Earthquake magnitude–time (M–t) plot for the region located in the southeastern wing of the Xinfengjiang Reservoir area. This region is marked by the red box in (d) and (e). (c) Cumulative number and magnitude of earthquakes shown in the shading period in (b). (d) Spatial distribution of earthquakes one month after the M7.7 mainshock. (e) Spatial distribution of earthquakes one year before the M7.7 mainshock.

close-examination of the first few seconds of the near-field seismogram revealed a possible small $\sim M6$ event with a slightly different focal mechanism right before the main slip pulse (Fig. 6). It is interesting to note that the TMD location of the M7.7 mainshock was about 40 km south of the USGS location, and about 20 km away from the Sagaing Fault. However, the latitude of the mainshock location from the TMD catalog agreed well with the relocation from another effort (Wei et al., 2025), although their longitudes differ by 15 km. A systematic shift of the TMD catalog to the right side is possible, likely due to the one-side network location. Relocations from our efforts (Fig. 6) are in between these hypocenters (Fig. 4b), suggesting that the mainshock likely started at least 20–30 km south of the USGS location. While such a number might be trivial for a 500-km-long rupture, it may affect some conclusions (e.g., subshear vs supershear) that depend strongly on the mainshock hypocenter location (e.g., Hirano et al., 2025; Zhang et al., 2025). In addition, local/regional observations can often see the initial event that is likely blurred or unresolvable at teleseismic distances (e.g., the M5.9 immediate foreshock or beginning of the mainshock about 14 s right before the 2025 M7.5 Noto earthquake (Peng et al., 2025)). Hence, we argue that when possible, local/regional hypocentral solutions should be used, rather than the default solutions from global observations.

A significant portion of aftershocks were shifted to the right side of the Sagaing Fault in the Shan Plateau (Fig. 4). However, large aftershocks from the USGS catalog were mostly on or very close to the Sagaing Fault (Fig. 4d). As noted before, at least part of the shift can be explained by the one-side station distribution of the TMD catalog.

However, the average shift (by assuming that the USGS location is accurate) is about 25 km (Fig. 4f), which cannot completely explain all aftershocks with some of them extending more than 75 km to the east of the Sagaing Fault (near the mainshock hypocenter). A simple explanation of those off-fault aftershocks can be reactivation of subsidiary faults within or near the Shan Plateau such as the Shan Scarp Fault (Bertrand et al., 1999), which are oriented at a certain angle to the Sagaing Fault. The beginning of the mainshock also likely occurred on such a subsidiary fault (Figs. 6 and 13). Such an off-fault aftershock activation would be more prominent especially during the supershear rupture segments of previous large strike-slip earthquakes (Bouchon and Karabulut, 2008). An alternative explanation would be that the Sagaing Fault is dipping to the east, which is consistent with inversions of GNSS observations (Tin et al., 2022) and microseismicity (Mon et al., 2020; Yang et al., 2024) before the M7.7 mainshock. Although some finite-fault inversions argued for a near-vertical rupture (Goldberg et al., 2025; Wei et al., 2025), results from inversions of the W-phase indicates the mainshock fault plane dipped significantly to the east near the mainshock hypocenter (Ye et al., 2025). Note that most aftershocks are in the apparent stress shadow of the mainshock (for either N-S striking or E-W striking fault) (Fig. 8 and S3, and Toda and Stein (2025)). Hence, these aftershocks cannot be simply explained by the clastic Coulomb stress changes (e.g. Stein, 1999) without consideration of sub faults having different strike and dip angles (Fig. 9). Instead, they are likely triggered by dynamic stress changes from the mainshock rupture or quasi-static stress changes following the mainshock (Freud, 2005).

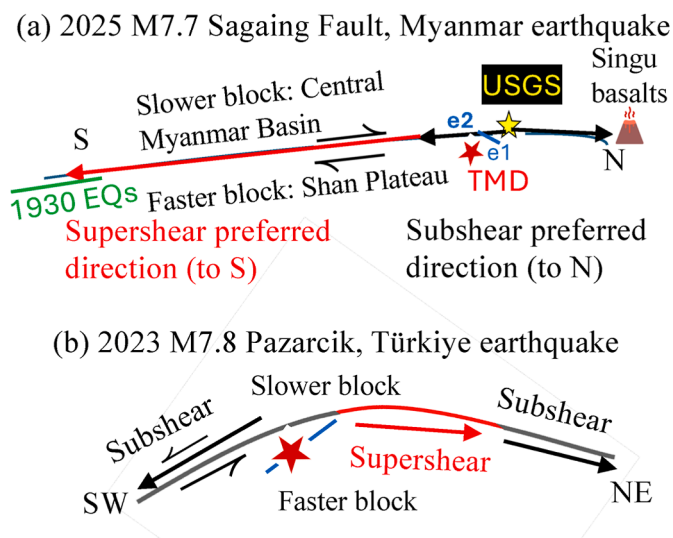


Fig. 13. A comparison of a relatively simple rupture for the 2025 M7.7 Sagaing Fault earthquake in Myanmar (a), and a slightly complicated rupture for the 2023 M7.8 Pazarcik earthquake along the East Anatolian Fault in Southcentral Türkiye (b). The red lines mark the sections where the rupture went supershear. The preferred direction for subshear rupture is to the slip direction of the side with lower seismic velocity, while the preferred direction for supershear is to the slip direction of the faster side (Ben-Zion and Shi, 2005). Yellow and red stars mark the hypocentral locations from the USGS and TMD, respectively. The relative locations of the two sub-events are marked as e1 and e2. Panel (b) is from Peng et al. (2025).

Our observation argues for an initial \sim M6 event on a subsidiary fault before jumping onto the main N-S striking Sagaing Fault (Fig. 13a). In this case, it is consistent with the inference that large strike-slip earthquakes tend to initiate from a subsidiary fault before migrating to the biomaterial fault interface (Brietzke and Ben-Zion, 2006; Stein and Bird, 2024). Such interpretation is also similar to the M4.7 foreshock occurring on a conjugated fault before the 2010 M6.7 Yushu earthquake within the Tibetan plateau (Chuang et al., 2023). The only difference is that the time separation between the foreshock and the mainshock for the Yushu sequence is about 2 h, while in this case, the time delay is only 3 s. Hence, it can be recognized as an immediate foreshock, such as the M5.9 foreshock \sim 14 s before the 2024 M7.6 Noto Peninsula earthquake in western Japan (Peng et al., 2025), or the ‘nucleation’ of the mainshock rupture such as the initial rupture of the 2023 M7.8 Pazarcik earthquake (Peng et al., 2025; Peng and Lei, 2025) or the 2024 M7.6 Noto mainshock (Ma et al., 2024). Note that almost all large earthquakes started with a relatively small event (i.e., the seismic nucleation phase) (Ellsworth and Beroza, 1995; Ide, 2014). Finally, the USGS- and the TMD-determined (probably assumed) initial hypocentral depths are both 10 km. Our newly determined focal depths for e1 and e2 are \sim 19 km and 24 km, respectively (Table S3), close to the lower boundary of coseismic slip distribution determined by the USGS (Goldberg et al., 2025) and other slip distributions (e.g., Wei et al., 2025; Inoue et al., 2025). Due to the lack of seismic stations right on top of the hypocenter, none of these determinations are accurate.

Despite possible complications in the initial mainshock rupture, the main ruptured fault segment is very simple without obvious fault kinks or step overs (Wei et al., 2025; Li et al., 2025). The mainshock first ruptured towards north along the Sagaing Fault for about 100 km with a subshear velocity (Fig. 2). The southward rupture also started with a subshear velocity for about 100 km, and then the rupture went supershear for another 300 km (Fig. 2) (Wei et al., 2025). However, Li et al. (2025) argued that the supershear ruptures started immediately south of the mainshock epicenter. The northward rupture ended near the Singu Plateau, which likely acted as a geometric barrier for the 1946 M7.7

earthquake, the 2012 Mw 6.8 Thabeikkyin earthquake and the 2025 M7.7 mainshock rupture (Antoine et al., 2025; Wei et al., 2025). The southern end of the 2025 rupture zone partially overlaps with the rupture zones of several M6-7 earthquakes in 1929–1930 (Wang et al., 2014; Wei et al., 2025). The arresting mechanism is more likely due to limited prestress instead of geometric complexity. In summary, the 2025 M7.7 mainshock rupture likely represent one end-member model of large continental strike-slip fault with very simple geometry (Fig. 13a) and no obvious branching or subsidiary fault ruptures. Another example of this type includes the 1906 M7.9 San Francisco earthquake (Song et al., 2008). The other end-member model would be the complex fault rupture such as the 2023 M7.8 Pazarcik earthquakes (Fig. 13b) and other events documented in Stein and Bird (2024).

Recent permanent and temporary seismic deployments across and along the Sagaing Fault have resulted in high-resolution imaging of subsurface crustal structures on both sides of the faults. These studies found that in the top few kms of the crust, the CMB in the Burma plate on the left side of the Sagaing Fault has slower seismic velocities than the Shan Plateau in the Sunda plate on the right side (Wang et al., 2019; Wu et al., 2021; Yao et al., 2022). Our initial observation of possible fault zone head waves at station GE.NPW (Fig. 7) also confirmed that the CWB side has slower velocity than the Shan Plateau. The existence of such a bi-material fault interface is expected to affect many aspects of earthquake source properties, including generation of a preferred rupture direction in the slip direction of the slower/more compliant block for a subshear rupture (e.g., Ben-Zion, 2001; Ampuero and Ben-Zion, 2008). For a supershear rupture, the propagation direction is flipped (i.e., in the slip direction of the faster/stiffer side) (Weertman, 2002; Shi and Ben-Zion, 2006). In addition to the ‘preferred’ rupture direction, dynamic ruptures on bi-material interface can generate asymmetric fault damage zone at depth (Ben-Zion and Shi, 2005). For a subshear rupture, the ‘preferred’ off-fault damage is on the stiffer side (Xu et al., 2012; Jara et al., 2021; Song et al., 2022), while the pattern is flipped again for the supershear rupture (i.e., on the more compliant side). We note that the northward rupture along the Sagaing Fault is subshear, matching the preferred slip direction of the slow CMB block, while the southward supershear rupture also matched the preferred slip direction of the fast Shan Plateau block (Fig. 13a). However, there existed a \sim 100 km southward subshear rupture that did not match this expectation. It is possible that the rupture had to start from subshear for a certain distance before jumping onto supershear speed. Additional seismic imaging studies at a finer scale (combined with fault zone head waves as observed in Fig. 7) can help to resolve whether the velocity contrast could be flipped in this section (e.g., Bennington et al., 2013). In addition, high-resolution optical imagery from Sentinel-2 displacement fields has been used to infer the co-seismic damage zones of \sim 100 m width following the M7.7 mainshock (Wei et al., 2025). However, no asymmetric fault damage zone has been inferred so far, likely due to the lack of accurate surface rupture traces. Additional surveys from in-situ field or remote satellite observations (Xu et al., 2025a, b, c; Zhang et al., 2025), together with dense cross-fault seismic arrays (Zor et al., 2025), can be used to further constrain the low-velocity damage zones at depth, and their relationship with dynamic earthquake ruptures.

We document clear evidence of remotely triggered seismicity near the border between Thailand and Myanmar, nearby Yunnan province in China, and the Xinfengjiang Reservoir in the Guangdong province in South China (Figs. 10–12). In most cases, seismicity started during and immediately following the large-amplitude surface waves, although in most cases large local events typically occurred a few hours to days following the mainshock, likely representing delayed dynamic triggering (Pollitz et al., 2012; Johnson and Bürgmann, 2016). In addition, many regions are a few fault lengths away from the M7.7 mainshock, where static stress changes became much lower than the dynamic stress changes. However, some regions, such as the border between Thailand and Myanmar are relatively close to the M7.7 mainshock rupture and hence could be affected by the static stress changes. While we do not

have the focal mechanisms of most triggered earthquakes, focal mechanisms of moderate-size events in this region are mostly N-S or E-W strike slip, which would receive negative ΔCFS (i.e., stress shadow) from the M7.7 mainshock slip (Fig. 8). This observation is consistent with other recent observations where microearthquakes in the static stress shadow of a mainshock can be instantaneously or delayed triggered by the dynamic stresses of the same mainshock rupture (Ma et al., 2005; Meng and Peng, 2014; Hardebeck and Harris, 2022; Yun et al., 2025). It would be interesting to observe whether in the long-term (i.e., after a few months when the effect of the dynamic stress is over), seismicity in the surrounding region would match with the prediction from the static stress changes from the M7.7 mainshock (Li et al., 2025; Toda and Stein, 2025).

Finally, we note that this section that ruptured during the M7.7 mainshock has long been recognized as a region that is long due for a major earthquake (Wang et al., 2014; Xiong et al., 2017; Habbard and Bradley, 2025). Although the location and its magnitude (to a less degree) can be anticipated, at this point we cannot accurately predict the timing of such a major earthquake. In addition, while the mainshock timing might be promoted by the tidal stresses (Fig. 8), there was no obvious foreshocks or other abnormal behaviors (at least seismically). The lack of reliable precursory signals highlights the challenge that earthquake scientists has been facing in the last half a century since the prediction of the 1975 Ms7.3 Haicheng earthquake (Wang et al., 2006; Peng and Lei, 2025). Nevertheless, multiple groups have deployed both permanent seismic network and temporary seismic arrays across and along the Sagaing Fault in the past decade (Thiam et al., 2017; Wang et al., 2019; Wu et al., 2021; Yao et al., 2022). Unfortunately, none of those temporary seismic arrays were active in 2025, and only 4 of the 9 stations in the Myanmar National Seismic Network (netcode: MM) were in operation during the mainshock. Station GE.NPW operated by GFZ provided a clear single near-field recording of the mainshock ruptures (Fig. 5; Lai et al., 2025). Better understanding of the large earthquakes requires long-term deployment and investments of near-fault zone arrays (Ben-Zion et al., 2022), possibly including on-fault motion-sensor cameras and video recordings (Chen et al., 2025; Latour et al., 2025; Hirano et al., 2025; Kearsse and Kaneko, 2025; Zhang et al., 2025; Xu et al., 2025b) and earthquake experiment sites (Wu, 2022) at regions where large earthquakes are due. These include regions such as the North-South Seismic Belt in China (Wu, 2022), the Southern Section of the San Andreas Fault (Fialko, 2006) and the Marmara Sea section of the North Anatolian Fault (NAF) near Istanbul (Becker et al., 2023).

CRedit authorship contribution statement

Zhigang Peng: Writing – original draft, Visualization, Supervision, Project administration, Methodology, Investigation, Funding acquisition, Formal analysis, Conceptualization. **Xinglin Lei:** Writing – review & editing, Visualization, Methodology, Investigation, Formal analysis. **Dun Wang:** Writing – review & editing, Visualization, Methodology, Formal analysis. **Xu Si:** Writing – review & editing, Visualization, Methodology, Investigation, Conceptualization. **Phuc Mach:** Writing – review & editing, Visualization, Methodology, Investigation, Formal analysis, Data curation. **Qiu Zhong:** Visualization, Formal analysis, Data curation. **Chang Ding:** Writing – review & editing, Visualization, Investigation, Formal analysis. **Yangfan Deng:** Writing – review & editing, Visualization, Methodology, Formal analysis, Data curation. **Min Qin:** Data curation. **Suqiu Miao:** Data curation.

Major points

1. The mainshock rupture is mainly supershear with surface rupture length of up to 500 km, resulting in one of the longest strike-slip rupture ever recorded.

2. Most aftershocks occurred in the eastern side of the Sagaing Fault, likely due to dipping of the mainshock fault plane and activation of the secondary faults.
3. This event triggered a widespread increase of microseismicity in Southeast Asia, some in the static stress shadow casted by the mainshock.

Declaration of competing interest

The authors declare the following financial interests/personal relationships which may be considered as potential competing interests: Given Dr. Zhigang Peng's role as Executive Editor-in-Chief, they had no involvement in the peer review of this article and had no access to information regarding its peer review. Full responsibility for the editorial process for this article was delegated to another journal editor. If there are other authors, they declare that they have no known competing financial interests or personal relationships that could have appeared to influence the work reported in this paper.

Acknowledgements

We thank the Thai Meteorological Department (TMD) for making their earthquake catalog available for this study. Most seismic data are downloaded from the Earthscope Inc. (formally known as IRIS)'s Data Management Center at the following website: https://ds.iris.edu/wilber3/find_stations/11952284. Waveform data from NPW can be retrieved from GEOFON using the FDSN. The velocity seismogram at station NPW is downloaded from <https://doi.org/10.5281/zenodo.15228691> (Bindi et al., 2025). Waveforms for the Yunnan network and earthquake catalogs in China are provided by the Yunnan and Guangdong Earthquake Agencies. Fig. 2 was produced by Mr. Yuyang Peng from Chinese University of Geosciences. We thank valuable comments and discussions with Professors Yehuda Ben-Zion, Shengji Wei, Jing Wu, Shiqing Xu and two anonymous reviewers. X.L is supported by the National Nonprofit Fundamental Research Grant of China, Institute of Geology, China Earthquake Administration (grant number IGCEA2504). Z.P., P.M., X.S. and C.D. are partially supported by National Science Foundation Grant RISE-2425889. Q.Z. is supported by Earthquake Prediction Open Fund, China Earthquake Administration (Grant No. XH25006D). Y.D. is supported by the International Partnership Program of Chinese Academy of Sciences (Grant No. 164GJHZ2023006MD).

Appendix A. Supplementary material

Supplementary material (three supplementary figures and three supplementary tables) to this article can be found online at <https://doi.org/10.1016/j.eqrea.2025.100413>.

References

- Allam, A.A., Ben-Zion, Y., Peng, Z., 2014. Seismic imaging of a bimaterial interface along the Hayward fault, CA, with fault zone head waves and direct P arrivals. *Pure Appl. Geophys.* 171, 2993–3011. <https://doi.org/10.1007/s00024-014-0784-0>.
- Ampuero, J.P., Ben-Zion, Y., 2008. Cracks, pulses and macroscopic asymmetry of dynamic rupture on a bimaterial interface with velocity-weakening friction. *Geophys. J. Int.* 173 (2), 674–692. <https://doi.org/10.1111/j.1365-246X.2008.03736.x>.
- Antoine, S.L., Shrestha, R., Milliner, C., Im, K., Rollins, C., Wang, K., Chen, K., Avouac, J. P., 2025. The 2025 Mw7.7 Mandalay, Myanmar, earthquake reveals a complex earthquake cycle with clustering and variable segmentation on the Sagaing Fault. *Proc. Natl. Acad. Sci.* 122 (33), e2514378122. <https://doi.org/10.1073/pnas.2514378122>.
- Becker, D., Martínez-Garzón, P., Wollin, C., Kılıç, T., Bohnhoff, M., 2023. Variation of fault creep along the overdue Istanbul-Marmara seismic gap in NW Türkiye. *Geophys. Res. Lett.* 50. <https://doi.org/10.1029/2022GL101471>.
- Bennington, N.L., Thurber, C., Peng, Z., Zhang, H., Zhao, P., 2013. Incorporating fault zone head wave and direct wave secondary arrival times into seismic tomography: application at Parkfield, California. *J. Geophys. Res.* 118, 1–7. <https://doi.org/10.1002/jgrb.50072>.
- Ben-Zion, Y., 2001. Dynamic ruptures in recent models of earthquake faults. *J. Mech. Phys. Solids* 49 (9), 2209–2244. [https://doi.org/10.1016/S0022-5096\(01\)00036-9](https://doi.org/10.1016/S0022-5096(01)00036-9).

- Ben-Zion, Y., Malin, P., 1991. San Andreas fault zone head waves near Parkfield, California. *Science* 251 (5001), 1592–1594. <https://doi.org/10.1126/science.251.5001.1592>.
- Ben-Zion, Y., Shi, Z., 2005. Dynamic rupture on a material interface with spontaneous generation of plastic strain in the bulk. *Earth Planet. Sci. Lett.* 236 (1–2), 486–496. <https://doi.org/10.1016/j.epsl.2005.03.025>.
- Ben-Zion, Y., Beroza, G.C., Bohnhoff, M., Gabriel, A.A., Mai, P.M., 2022. A grand challenge international infrastructure for earthquake science. *Seismol. Res. Lett.* 93 (6), 2967–2968. <https://doi.org/10.1785/0220220266>.
- Bertrand, G., Rangin, C., 2003. Tectonics of the western margin of the Shan plateau (central Myanmar): implication for the India–Indochina oblique convergence since the Oligocene. *J. Asian Earth Sci.* 21 (10), 1139–1157. [https://doi.org/10.1016/S1367-9120\(02\)00183-9](https://doi.org/10.1016/S1367-9120(02)00183-9).
- Bertrand, G., Rangin, C., Maluski, H., Han, T.A., Thein, M., Myint, O., Maw, W., Lwin, S., 1999. Cenozoic metamorphism along the Shan scarp (Myanmar): evidences for ductile shear along the Sagaing fault or the northward migration of the eastern Himalayan syntaxis? *Geophys. Res. Lett.* 26 (7), 915–918. <https://doi.org/10.1029/1999GL900136>.
- Bindi, D., Lai, S.-T., Strollo, A., Zaccarelli, R., Tilmann, F., 2025. Software and Data Products for "Capacity Building Enables Unique Near-Fault Observations of the Destructive 2025 Mw 7.7 Myanmar Earthquake. Zenodo. <https://doi.org/10.5281/zenodo.15228691>.
- Bouchon, M., Karabulut, H., 2008. The aftershock signature of supershear earthquakes. *Science* 320 (5881), 1323–1325. <https://doi.org/10.1126/science.1155030>.
- Bradley, K., Hubbard, J., 2024. The great tidal earthquake hypothesis test, part III. *Earthquake insights*. <https://doi.org/10.62481/3b93879a>.
- Bradley, K., Hubbard, J., 2025a. Updates on the M7.7 Myanmar earthquake. *Earthquake insights*. <https://doi.org/10.62481/9e49eb4a>.
- Bradley, K., Hubbard, J., 2025b. Surface ruptures of the Myanmar M7.7 earthquake mapped from space. *Earthquake Insights*. <https://doi.org/10.62481/51b7df8c>.
- Brietzeke, G.B., Ben-Zion, Y., 2006. Examining tendencies of in-plane rupture to migrate to material interfaces. *Geophys. J. Int.* 167 (2), 807–819. <https://doi.org/10.1111/j.1365-246X.2006.03137.x>.
- Cai, J., Xi, N., Han, G., Deng, W., Sun, L., 2025. Rapid report of the March 28, 2025 Mw 7.9 Myanmar earthquake. *Earthquake Res. Adv.*, 100396 <https://doi.org/10.1016/j.eqrea.2025.100396>.
- Chansom, C., Jitmahantakul, S., Owen, L.A., Wiwegwin, W., Charusiri, P., 2022. New insights into the paleoseismic history of the Mae Hong Son Fault, northern Thailand. *Front. Earth Sci.* 10, 921049. <https://doi.org/10.3389/feart.2022.921049>.
- Chen, K., Meng, H., Zhang, Z., Wang, Z., Liu, Z., Milliner, C., Wei, G., Zheng, Fu, Gao, J., Zhou, M., Antoine, S.L., Wang, C., He, Z., Huang, K., Song, J., Ma, Q., Luo, H., Chen, X., Avouac, J.-P., 2025. On-fault and remote observations of exceptionally long, supershear rupture in the 2025 M7.7 Mandalay earthquake. *Sci. Adv.* submitted for publication.
- Chuang, L.Y., Peng, Z., Lei, X., Wang, B., Liu, J., Zhai, Q., Tu, H., 2023. Foreshocks of the 2010 Mw 6.7 Yushu, China Earthquake occurred near an Extensional step-over. *J. Geophys. Res.* 128, e2022JB025176. <https://doi.org/10.1029/2022JB025176>.
- Crosetto, S., Watkinson, I.M., Min, S., Falcucci, E., Gori, S., Thein, P.S., Sudeep, 2019. Searching for the 1912 Maymyo earthquake: new evidence from paleoseismic investigations along the Kyaukkan Fault, Myanmar. *Quat. Int.* 532, 75–86. <https://doi.org/10.1016/j.quaint.2019.09.042>.
- Dziewonski, A., Hales, A., Lapwood, E., 1975. Parametrically simple Earth models consistent with geophysical data. *Phys. Earth Planet. Inter.* 10 (1), 12–48. [https://doi.org/10.1016/0031-9201\(75\)90017-5](https://doi.org/10.1016/0031-9201(75)90017-5).
- Ellsworth, W.L., Beroza, G.C., 1995. Seismic evidence for an earthquake nucleation phase. *Science* 268 (5212), 851–855. <https://doi.org/10.1126/science.268.5212.851>.
- Fialko, Y., 2006. Interseismic strain accumulation and the earthquake potential on the southern San Andreas fault system. *Nature* 441 (7096), 968–971. <https://doi.org/10.1038/nature04797>.
- Foulger, G.R., Wilson, M.P., Gluyas, J.G., Julian, B.R., Davies, R.J., 2018. Global review of human-induced earthquakes. *Earth Sci. Rev.* 178, 438–514. <https://doi.org/10.1016/j.earscirev.2017.07.008>.
- Freed, A.M., 2005. Earthquake triggering by static, dynamic, and postseismic stress transfer. *Annu. Rev. Earth Planet. Sci.* 33 (1), 335–367. <https://doi.org/10.1146/annurev.earth.33.092203.122505>.
- Gahalaut, V.K., Gahalaut, K., 2007. Burma plate motion. *J. Geophys. Res.* 112, B10402. <https://doi.org/10.1029/2007JB004928>.
- Goldberg, D.E., Yeck, W.L., Hanagan, C., Atterholt, J., Kehoe, H., Reitman, N., Barnhart, W.D., Shelly, D.R., Hatem, A.E., Wald, D., Earle, P.S., 2025. Ultralong, supershear rupture of the 2025 Mw7.7 Mandalay earthquake reveals unaccounted risk. *Science, revised*.
- Hardebeck, J.L., Harris, R.A., 2022. Earthquakes in the shadows: why aftershocks occur at surprising locations. *Seismic Record* 2 (3), 207–216. <https://doi.org/10.1785/0320220023>.
- Henry, C., Das, S., 2001. Aftershock zones of large shallow earthquakes: fault dimensions, aftershock area expansion and scaling relations. *Geophys. J. Int.* 147 (2), 272–293. <https://doi.org/10.1046/j.1365-246X.2001.00522.x>.
- Hill, D.P., Prejean, S.G., 2015. Dynamic triggering. In: *Treatise on Geophysics, Second Edition*, Elsevier, pp. 273–304. <https://doi.org/10.1016/b978-0-444-53802-4.00078-6>.
- Hirano, S., Doke, R., Maeda, T., 2025. Supershear-subshear-supershear rupture sequence during the 2025 Mandalay Earthquake in Myanmar. *Seismica* 4 (2). <https://doi.org/10.26443/seismica.v4i2.1785>.
- Hough, S.E., 2018. Do large (magnitude ≥ 8) global earthquakes occur on preferred days of the calendar year or lunar cycle? *Seismol. Res. Lett.* 89 (2A), 577–581. <https://doi.org/10.1785/0220170154>.
- Hu, X.P., Zang, A., Heidbach, O., Cui, X.F., Xie, F.R., Chen, J.W., 2017. Crustal stress pattern in China and its adjacent areas. *J. Asian Earth Sci.* 149, 20–28. <https://doi.org/10.1016/j.jseaes.2017.07.005>.
- Huang, R.Q., Deng, Y.F., Chen, Y., Xiong, C., Zhang, Z., 2025. Source parameters and stress triggering of 2023 $M \geq 4$ earthquakes sequence in Heyuan, Guangdong. *Chinese J. Geophys.* (in Chinese with English abstract) 68 (3), 956–969. <https://doi.org/10.6038/cjg2024R0701>.
- Hubbard, J., Bradley, K., 2025. Catastrophic M7.7 earthquake caused by rupture of Sagaing Fault in Myanmar. *Earthquake Insights*. <https://doi.org/10.62481/9250a38a>.
- Ide, S., 2014. Modeling fast and slow earthquakes at various scales. *Proc. Japan Acad. Series B* 90 (8), 259–277. <https://doi.org/10.2183/pjab.90.259>.
- Ide, S., Yabe, S., Tanaka, Y., 2016. Earthquake potential revealed by tidal influence on earthquake size–frequency statistics. *Nat. Geosci.* 9 (11), 834–837. <https://doi.org/10.1038/ngeo2796>.
- Inoue, N., Yamaguchi, R., Yagi, Y., Okuwaki, R., Bogdan, E., Tadapansawut, T., 2025. A multiple asymmetric bilateral rupture sequence derived from the peculiar teleseismic P-waves of the 2025 Mandalay, Myanmar earthquake. *Seismica* 4 (1). <https://doi.org/10.26443/seismica.v4i1.1691>.
- Iwata, T., 2008. Low detection capability of global earthquakes after the occurrence of large earthquakes: investigation of the Harvard CMT catalogue. *Geophys. J. Int.* 174 (3), 849–856. <https://doi.org/10.1111/j.1365-246X.2008.03864.x>.
- Jackson, D.D., Kagan, Y.Y., 2011. Characteristic earthquakes and seismic gaps. In: Gupta, H.K. (Ed.), *Encyclopedia of Solid Earth Geophysics*. Encyclopedia of Earth Sciences Series. Springer, Dordrecht. https://doi.org/10.1007/978-90-481-8702-7_181.
- Jara, J., Bruhat, L., Thomas, M.Y., Antoine, S.L., Okubo, K., Rougier, E., Rosakis, A.J., Sammis, C.G., Klüger, Y., Jolivet, R., Bhat, H.S., 2021. Signature of transition to supershear rupture speed in the coseismic off-fault damage zone. *Proc. Royal Soc. A* 477 (2255), 20210364. <https://doi.org/10.1098/rspa.2021.0364>.
- Johnson, C.W., Bürgmann, R., 2016. Delayed dynamic triggering: local seismicity leading up to three remote $M \geq 6$ aftershocks of the 11 April 2012 M8.6 Indian Ocean earthquake. *J. Geophys. Res.* 121, 134–151. <https://doi.org/10.1002/2015JB012243>.
- Kagan, Y.Y., 2004. Short-term properties of earthquake catalogs and models of earthquake source. *Bull. Seismol. Soc. Am.* 94 (4), 1207–1228. <https://doi.org/10.1785/012003098>.
- Kagan, Y.Y., Jackson, D.D., Geller, R.J., 2012. Characteristic earthquake model, 1884–2011, RIP. *arXiv preprint*. <https://arxiv.org/pdf/1207.4836>.
- Kearse, J., Kaneko, Y., 2025. Curved fault slip captured by CCTV video during the 2025 M w 7.7 Myanmar Earthquake. *Seismic Record* 5 (3), 281–288. <https://doi.org/10.1785/0320250024>.
- Kiser, E., Ishii, M., 2017. Back-projection imaging of earthquakes. *Annu. Rev. Earth Planet. Sci.* 45 (1), 271–299. <https://doi.org/10.1146/annurev-earth-063016-015801>.
- Kwiatk, G., Martínez-Garzón, P., Becker, D., Dresen, G., Cotton, F., Beroza, G.C., Acael, D., Ergintav, S., Bohnhoff, M., 2023. Months-long seismicity transients preceding the 2023 MW 7.8 Kahramanmaraş earthquake, Türkiye. *Nat. Commun.* 14 (1), 7534. <https://doi.org/10.1038/s41467-023-42419-8>.
- Lai, S.T., Oo, K.M., Htw, Y.M.M., Yi, T., Than, H.H., Than, O., Min, Z., Oo, T.M., Maung, P.M., Bindi, D., Cotton, F., 2025. Capacity building enables unique near-fault observations of the destructive 2025 M w 7.7 Myanmar Earthquake. *Earth Syst. Sci. Data Discuss.* <https://doi.org/10.5194/essd-2025-216> submitted for publication.
- Latour, S., Lebihain, M., Bhat, H.S., Twardzik, C., Bletery, Q., Hudnut, K.W., Passetegue, F., 2025. Direct estimation of earthquake source properties from a single CCTV camera. <https://arxiv.org/abs/2505.15461>.
- Lei, X., Xie, C., Fu, B., 2011. Remotely triggered seismicity in Yunnan, southwestern China, following the 2004 Mw9.3 Sumatra earthquake. *J. Geophys. Res.* 116, B08303. <https://doi.org/10.1029/2011JB008245>.
- Lengine, O., Enescu, B., Peng, Z., Shiomi, K., 2012. Decay and migration of the early aftershock activity following the Tohoku Mw9.0 2011 earthquake. *Geophys. Res. Lett.* 39, L18309. <https://doi.org/10.1029/2012GL052797>.
- Li, L., Wang, B., Peng, Z., Li, D., 2019. Dynamic triggering of microseismicity in Southwest China following the 2004 Sumatra and 2012 Indian Ocean earthquakes. *J. Asian Earth Sci.* 176, 129–140. <https://doi.org/10.1016/j.jseaes.2019.02.010>.
- Li, T., Song, X., 2025. Moment Magnitude of Myanmar Earthquake on March 28, 2025 from long-period seismic coda. *Earthq. Sci.* <https://doi.org/10.2139/ssrn.5220290> accepted.
- Li, Y., Yang, C., Hu, X., Yuan, J., Yao, G., Li, H., 2025. Coulomb stress transfer from the 2025 Mw 7.7 Myanmar earthquake to active faults in Southwestern Yunnan, China: implications for seismic hazard. *Earthq. Res. Adv.* <https://doi.org/10.1016/j.eqrea.2025.100397> accepted.
- Liao, Y.C., Kao, H., Rosenberger, A., Hsu, S.K., Huang, B.S., 2012. Delineating complex spatiotemporal distribution of earthquake aftershocks: an improved source-scanning algorithm. *Geophys. J. Int.* 189 (3), 1753–1770. <https://doi.org/10.1111/j.1365-246X.2012.05457.x>.
- Lindsey, E.O., Wang, Y., Aung, L.T., Chong, J.H., Qiu, Q., Mallick, R., Feng, L., Aung, P. S., Tin, T.Z.H., Min, S.M., Bradley, K., 2023. Active subduction and strain partitioning in western Myanmar revealed by a dense survey GNSS network. *Earth Planet. Sci. Lett.* 622, 118384. <https://doi.org/10.1016/j.epsl.2023.118384>.
- Ma, K.-F., Chan, C.-H., Stein, R.S., 2005. Response of seismicity to Coulomb stress triggers and shadows of the 1999 Mw = 7.6 Chi-Chi, Taiwan, earthquake. *J. Geophys. Res.* 110, B05S19. <https://doi.org/10.1029/2004JB003389>.

- Ma, Z., Zeng, H., Luo, H., Liu, Z., Jiang, Y., Aoki, Y., Wang, W., Itoh, Y., Lyu, M., Cui, Y., Yun, S.H., Hill, E.M., Wei, S., 2024. Slow rupture in a fluid-rich fault zone initiated the 2024 M 7.5 Noto earthquake. *Science* 385 (6711), 866–871. <https://doi.org/10.1126/science.ado5143>.
- Mallick, R., Lindsey, E.O., Feng, L., Hubbard, J., Banerjee, P., Hill, E.M., 2019. Active convergence of the India–Burma–Sunda plates revealed by a new continuous GPS network. *J. Geophys. Res.* 124, 3155–3171. <https://doi.org/10.1029/2018JB016480>.
- Matsumoto, K., Sato, T., Takanezawa, T., Ooe, M., 2001. GOTIC2: a program for computation of oceanic tidal loading effect. *J. Geod. Soc. Jpn.* 47, 243–248. <https://doi.org/10.11366/sokuchi1954.47.243>.
- McCaffrey, R., 2009. The tectonic framework of the Sumatran subduction zone. *Annu. Rev. Earth Planet Sci.* 37 (1), 345–366. <https://doi.org/10.1146/annurev.earth.031208.100212>.
- Melgar, D., Weldon, R., Wang, Y., Bato, M.G., Aung, L.T., Shi, X., Wiwegwing, W., Khaing, S.N., Min, S., Thant, M., Speed, C., Zinke, R., Fielding, E., Meltzner, A., Dawson, T., 2025. Supershear source model of the 2025 M7.8 Myanmar earthquake and paleoseismology of the Sagaing Fault: regions of significant overlap with past earthquakes. *Seismica* 4 (2). <https://doi.org/10.26443/seismica.v4i2.1771>.
- Meng, X., Peng, Z., 2014. Seismicity rate changes in the San Jacinto fault zone and the Salton Sea Geothermal field following the 2010 Mw7.2 El Mayor-Cucapah Earthquake. *Geophys. J. Int.* 197 (3), 1750–1762. <https://doi.org/10.1093/gji/ggu085>.
- Mogi, K., 1979. Two kinds of seismic gaps. *Pure Appl. Geophys.* 117 (6), 1172–1186. <https://doi.org/10.1007/BF00876213>.
- Mon, C.T., Gong, X., Wen, Y., Jiang, M., Chen, Q.F., Zhang, M., Hou, G., Thant, M., Sein, K., He, Y., 2020. Insight into major active faults in Central Myanmar and the related geodynamic sources. *Geophys. Res. Lett.* 47, e2019GL086236. <https://doi.org/10.1029/2019GL086236>.
- Nielsen, C., Chamot-Rooke, N., Rangin, C., The ANDAMAN Cruise Team, 2004. From partial to full strain partitioning along the Indo-Burmese hyper-oblique subduction. *Mar. Geol.* 209, 303–327. <https://doi.org/10.1016/j.margeo.2004.05.001>.
- Ozacar, A.A., Beck, S.L., 2004. The 2002 Denali fault and 2001 Kunlun fault earthquakes: complex rupture processes of two large strike-slip events. *Bull. Seismol. Soc. Am.* 94 (6B), S278–S292. <https://doi.org/10.1785/0120040604>.
- Peng, Z., Chao, K., 2008. Non-volcanic tremor beneath the Central range in Taiwan triggered by the 2001 Mw7.8 Kunlun earthquake. *Geophys. J. Int.* 175, 825–829. <https://doi.org/10.1111/j.1365-246X.2008.03886.x>.
- Peng, Z., Zhao, P., 2009. Migration of early aftershocks following the 2004 Parkfield earthquake. *Nat. Geosci.* 2, 877–888. <https://doi.org/10.1038/ngeo697>.
- Peng, Z., Gombert, J., 2010. An integrated perspective of the continuum between earthquakes and slow-slip phenomena. *Nat. Geosci.* 3, 599–607. <https://doi.org/10.1038/ngeo940>.
- Peng, Z., Lei, X., 2025. Physical mechanisms of earthquake nucleation and foreshock cascade triggering, aseismic slip, or fluid flows? *Earthq. Res. Adv.* 5 (2), 100349. <https://doi.org/10.1016/j.eqrea.2024.100349>.
- Peng, Z., Vidale, J.E., Houston, H., 2006. Anomalous early aftershock decay rates of the 2004 M6 Parkfield earthquake. *Geophys. Res. Lett.* 33, L17307. <https://doi.org/10.1029/2006GL026744>.
- Peng, Z., Lei, X., Wang, Q.-Y., Wang, D., Mach, P., Yao, D., Kato, A., Obara, K., Campillo, M., 2025. The evolution process between the earthquake swarm beneath the Noto peninsula, central Japan and the 2024 M 7.6 Noto Hanto earthquake sequence. *Earthq. Res. Adv.* 5 (1), 100332. <https://doi.org/10.1016/j.eqrea.2024.100332>.
- Prejean, S.G., Hill, D.P., Brodsky, E.E., Hough, S.E., Johnston, M.J.S., Malone, S.D., Oppenheimer, D.H., Pitt, A.M., Richards-Dinger, K.B., 2004. Remotely triggered seismicity on the United States West Coast following the Mw 7.9 Denali Fault earthquake. *Bull. Seismol. Soc. Am.* 94 (6B), S348–S359. <https://doi.org/10.1785/0120040610>.
- Pollitz, F.F., Stein, R.S., Sevilgen, V., Bürgmann, R., 2012. The 11 April 2012 east Indian Ocean earthquake triggered large aftershocks worldwide. *Nature* 490 (7419), 250–253. <https://doi.org/10.1038/nature11504>.
- Rangin, C., Maurin, T., Masson, F., 2013. Combined effects of Eurasia/Sunda oblique convergence and East-Tibetan crustal flow on the active tectonics of Burma. *J. Asian Earth Sci.* 76, 185–194. <https://doi.org/10.1016/j.jseaes.2013.05.018>.
- Ren, C., Wang, Z., Taymaz, T., Hu, N., Luo, H., Zhao, Z., Yue, H., Song, X., Shen, Z., Xu, H., Geng, J., 2024. Supershear triggering and cascading fault ruptures of the 2023 Kahramanmaraş, Türkiye, earthquake doublet. *Science* 383 (6680), 305–311. <https://doi.org/10.1126/science.adil1519>.
- Robinson, D.P., Das, S., Searle, M.P., 2010. Earthquake fault superhighways. *Tectonophysics* 493 (3–4), 236–243. <https://doi.org/10.1016/j.tecto.2010.01.010>.
- Ruan, Y., 2007. *Source Parameters and Triggering Mechanism of the Nansang Earthquake Triggered by the Sumatra Earthquake*. University of Science and Technology of China, p. 59. M.S. Thesis.
- Song, B.R., Song, W.J., Johnson, S.E., Gerbi, C.C., Vel, S.S., 2022. Elastic contrast, rupture directivity, and damage asymmetry in an anisotropic bimaterial strike-slip fault at the middle crustal depths. *J. Geophys. Res.* 127, e2021JB023821. <https://doi.org/10.1029/2021JB023821>.
- Song, S.G., Beroza, G.C., Segall, P., 2008. A unified source model for the 1906 San Francisco earthquake. *Bull. Seismol. Soc. Am.* 98 (2), 823–831. <https://doi.org/10.1785/0120060402>.
- Shahzada, K., Noor, U.A., Xu, Z.D., 2025. In the Wake of the March 28, 2025 Myanmar Earthquake: a Detailed Examination. *J. Dynamic Disasters* 1 (2), 100017. <https://doi.org/10.1016/j.jdd.2025.100017>.
- Shi, Z., Ben-Zion, Y., 2006. Dynamic rupture on a bimaterial interface governed by slip-weakening friction. *Geophys. J. Int.* 165 (2), 469–484. <https://doi.org/10.1111/j.1365-246X.2006.02853.x>.
- Stein, R.S., 1999. The role of stress transfer in earthquake occurrence. *Nature* 402, 605–609. <https://doi.org/10.1038/45144>.
- Stein, R.S., Bird, P., 2024. Why do great continental transform earthquakes nucleate on branch faults? *Seismol. Res. Lett.* 95 (6), 3406–3415. <https://doi.org/10.1785/0220240175>.
- Tanaka, S., 2012. Tidal triggering of earthquakes prior to the 2011 Tohoku-Oki earthquake (Mw 9.1). *Geophys. Res. Lett.* 39, 00G26. <https://doi.org/10.1029/2012GL015179>.
- Thiam, H.N., Htwe, Y.M.M., Kyaw, T.L., Tun, P.P., Min, Z., Htwe, S.H., Aung, T.M., Lin, K.K., Aung, M.M., Cristofaro, J.D., Franke, M., 2017. A report on upgraded seismic monitoring stations in Myanmar: station performance and site response. *Seismol. Res. Lett.* 88 (3), 926–934. <https://doi.org/10.1785/0220160168>.
- Timsina, P., Hearn, T.M., Ni, J.F., 2024. Crust and mantle flow from central Tibetan Plateau to the Indo-Burma subduction zone. *J. Geophys. Res.* 129, e2023JB027540. <https://doi.org/10.1029/2023JB027540>.
- Tin, T.Z.H., Nishimura, T., Hashimoto, M., Lindsey, E.O., Aung, L.T., Min, S.M., Thant, M., 2022. Present-day crustal deformation and slip rate along the southern Sagaing fault in Myanmar by GNSS observation. *J. Asian Earth Sci.* 228, 105125. <https://doi.org/10.1016/j.jseaes.2022.105125>.
- Toda, S., Stein, R.S., 2025. One-month earthquake forecast for western Myanmar following the devastating magnitude 7.7 Mandalay shock, Temblor. <http://doi.org/10.32858/temblor.360>.
- Tun, S.T., Watkinson, I.M., 2017. Chapter 19: the Sagaing Fault, Myanmar. In: Barber, A. J., Zaw, K., Crow, M.J. (Eds.), Myanmar: Geology, Resources and Tectonics. Geological Society, London, Memoirs. <https://doi.org/10.1144/m48.19>.
- Utsu, T., Ogata, Y., Matsuura, R.S., 1995. The centenary of the Omori formula for a decay law of aftershock activity. *J. Phys. Earth* 43 (1), 1–33. <https://doi.org/10.4294/jpe1952.43.1>.
- Vera, F., Carrillo-Ponce, A., Crosetto, S., Kosari, E., Metzger, S., Motagh, M., Liang, Y., Lyu, S., Petersen, G., Saul, J., Sudhaus, H., 2025. Supershear Rupture Along the Sagaing Fault Seismic Gap: The 2025 Myanmar Earthquake. *Seismic Record* 5 (3), 289–299. <https://doi.org/10.1785/0320250025>.
- Wald, D.J., Worden, C.B., Thompson, E.M., Hearne, M., 2022. ShakeMap operations, policies, and procedures. *Earthq. Spectra* 38 (1), 756–777. <https://doi.org/10.1177/87552930211030298>.
- Wang, D., Mori, J., 2011. Rupture process of the 2011 off the Pacific coast of Tohoku Earthquake (Mw 9.0) as imaged with back-projection of teleseismic P-waves. *Earth Planets Space* 63, 603–607. <https://doi.org/10.5047/eps.2011.05.029>.
- Wang, D., Kawakatsu, H., Mori, J., Ali, B., Ren, Z., Shen, X., 2016a. Backprojection analyses from four regional arrays for rupture over a curved dipping fault: the Mw 7.7 24 September 2013 Pakistan earthquake. *J. Geophys. Res.* 121 (3), 1948–1961. <https://doi.org/10.1002/2015JB012168>.
- Wang, D., Mori, J., Koketsu, K., 2016b. Fast rupture propagation for large strike-slip earthquakes. *Earth Planet Sci. Lett.* 440, 115–126. <https://doi.org/10.1016/j.epsl.2016.02.022>.
- Wang, Y., Sieh, K., Tun, S.T., Lai, K.Y., Myint, T., 2014. Active tectonics and earthquake potential of the Myanmar region. *J. Geophys. Res.* 119, 3767–3822. <https://doi.org/10.1002/2013JB010762>.
- Wang, X., Wei, S., Wang, Y., Maung Maung, P., Hubbard, J., Banerjee, P., Huang, B.S., Moe Oo, K., Bodin, T., Foster, A., Almeida, R., 2019. A 3-D shear wave velocity model for Myanmar region. *J. Geophys. Res.* 124, 504–526. <https://doi.org/10.1029/2018JB016622>.
- Weertman, J., 2002. Subsonic type earthquake dislocation moving at approximately \times shear wave velocity on interface between half spaces of slightly different elastic constants. *Geophys. Res. Lett.* 29 (10). <https://doi.org/10.1029/2001GL013916>.
- Wei, S., Wang, X., Li, C., et al., 2025. Supershear Rupture sustained through a thick fault zone in the 2025 Mw 7.8 Myanmar Earthquake. *Science revised*.
- Wells, D.L., Coppersmith, K.J., 1994. New empirical relationships among magnitude, rupture length, rupture width, rupture area, and surface displacement. *Bull. Seismol. Soc. Am.* 84 (4), 974–1002. <https://doi.org/10.1785/BSSA0840040974>.
- Weng, H., Ampuero, J.-P., 2019. The dynamics of elongated earthquake ruptures. *J. Geophys. Res.* 124, 8584–8610. <https://doi.org/10.1029/2019JB017684>.
- Wesnously, S.G., 2006. Predicting the endpoints of earthquake ruptures. *Nature* 444 (7117), 358–360. <https://doi.org/10.1038/nature05275>.
- Wu, Z., 2022. Seismic experimental sites: challenges and opportunities. In: Li, Y.G., Zhang, Y., Wu, Z. (Eds.), China Seismic Experimental Site. Springer, Singapore. https://doi.org/10.1007/978-981-16-8607-8_1.
- Wu, S., Yao, J., Wei, S., Hubbard, J., Wang, Y., Htwe, Y.M.M., Thant, M., Wang, X., Wang, K., Liu, T., Liu, Q., 2021. New insights into the structural heterogeneity and geodynamics of the Indo-Burma subduction zone from ambient noise tomography. *Earth Planet Sci. Lett.* 562, 116856. <https://doi.org/10.1016/j.epsl.2021.116856>.
- Xiong, X., Shan, B., Zhou, Y.M., Wei, S.J., Li, Y.D., Wang, R.J., Zheng, Y., 2017. Coulomb stress transfer and accumulation on the Sagaing Fault, Myanmar, over the past 110 years and its implications for seismic hazard. *Geophys. Res. Lett.* 44, 4781–4789. <https://doi.org/10.1002/2017GL072770>.
- Xu, D., Luo, H., Yu, H., Peng, Z., Zhu, H., Xu, J., Jiao, L., Dong, S., Bao, Gu, Ren, Z., Chen, X., 2025a. Sediments-modulated supershear rupture of the 2025 Mw 7.7 Myanmar earthquake. *Commun. Earth Environ.* submitted for publication.
- Xu, J., Zhang, H., Chen, X., 2015. Rupture phase diagrams for a planar fault in 3-D full-space and half-space. *Geophys. J. Int.* 202 (3), 2194–2206. <https://doi.org/10.1093/gji/ggv284>.
- Xu, L., Mohanna, S., Meng, L., Ji, C., Ampuero, J.P., Yunjun, Z., Hasnain, M., Chu, R., Liang, C., 2023. The overall-supershear and multi-segment rupture of the 2023 Mw7.8

- Kahramanmaraş, Turkey earthquake in millennia supercycle. *Commun. Earth Environ.* 4 (1), 379. <https://doi.org/10.1038/s43247-023-01030-x>.
- Xu, L., Meng, L., Zhang, Y., et al., 2025b. Bimaterial effect and favorable energy ratio enable supershear Rupture in the 2025 Myanmar Quake. *Science* in revision.
- Xu, S., Ben-Zion, Y., Ampuero, J.-P., 2012. Properties of inelastic yielding zones generated by in-plane dynamic ruptures: II. Detailed parameter-space study. *Geophys. J. Int.* 191, 1343–1360. <https://doi.org/10.1111/j.1365-246X.2012.05685.x>.
- Xu, X., Kang, W., Wang, T., Zhang, X., Liu, Y., Zhang, Y., Zhao, J., Li, K., Wang, Q., Cheng, J., Ren, J., 2025c. The Mw7.7 Myanmar earthquake: a continental longest surface-rupturing supershear cascading event. *npj Natural Hazards* 2, 73. <https://doi.org/10.1038/s44304-025-00125-z>.
- Yang, S., Xiao, Z., Wei, S., He, Y., Mon, C.T., Hou, G., Thant, M., Sein, K., Jiang, M., 2024. New insights into active faults revealed by a deep-learning-based earthquake catalog in central Myanmar. *Geophys. Res. Lett.* 51, e2023GL105159. <https://doi.org/10.1029/2023GL105159>.
- Yao, H., 2020. Building the community velocity model in the Sichuan-Yunnan region, China: Strategies and progresses. *Science China Earth Sciences* 63 (9), 1425–1428. <https://doi.org/10.1007/s11430-020-9645-3>.
- Yao, D., Peng, Z., Ding, C., Sandvol, E., Godoladze, T., Yetirmishli, G., 2024. Dynamically triggered tectonic tremors and earthquakes in the caucasian region following the 2023 Kahramanmaraş, Türkiye, earthquake sequence. *Geophys. Res. Lett.* 51, e2024GL110786. <https://doi.org/10.1029/2024GL110786>.
- Yao, J., Wu, S., Li, T., Bai, Y., Xiao, X., Hubbard, J., Wang, Y., Thant, M., Tong, P., 2022. Imaging the upper 10 km crustal shear-wave velocity structure of central Myanmar via a joint inversion of P-Wave polarizations and receiver functions. *Seismol Res. Lett.* 93, 1710–1720. <https://doi.org/10.1785/0220210292>.
- Yao, S., Yang, H., 2025. Rupture phases reveal geometry-related rupture propagation in a natural earthquake. *Sci. Adv.* 11 (4), eadq0154. <https://doi.org/10.1126/sciadv.adq0154>.
- Ye, L., Lay, T., Kanamori, H., 2025. The 28 March 2025 M w 7.8 Myanmar Earthquake: preliminary analysis of an ~480 km long intermittent supershear rupture. *Seismic Record* 5 (3), 260–269. <https://doi.org/10.1785/0320250021>.
- Yin, A., Harrison, T.M., 2000. Geologic evolution of the Himalayan-Tibetan orogen. *Annu. Rev. Earth Planet Sci.* 28 (1), 211–280. <https://doi.org/10.1146/annurev.earth.28.1.211>.
- Yu, Z., Wang, W., 2022. FastLink: a machine learning and GPU-based fast phase association method and its application to Yangbi Ms 6.4 aftershock sequences. *Geophys. J. Int.* 230 (1), 673–683. <https://doi.org/10.1093/gji/ggac088>.
- Yun, J., Gabriel, A.A., May, D.A., Fialko, Y., 2025. Controls of dynamic and static stress changes and aseismic slip on delayed earthquake triggering in rate-and-state simulations of the 2019 ridgecrest earthquake sequence. *J. Geophys. Res.* <https://doi.org/10.31223/X55983> submitted for publication.
- Zhang, F., Gao, J., Liu, Z., Meng, H., Wang, C., Wang, L., Hou, Y., Xu, S., Peng, Z., Yue, H., Sun, J., Zhou, M., Wang, Z., Ben-Zion, Y., 2025. Rich Rupture Dynamics of the 2025 Mw 7.7 Mandalay, Myanmar Earthquake Revealed by Unprecedented On-Fault Video and Additional Multimodal Observations. *Nature Geosci.* submitted for publication.
- Zhao, X., Meng, L., Peng, G., He, X., 2025. Aftershock evolution characteristics of the 28 March 2025 Mw7.7 Myanmar earthquake sequence. *Earthquake sciences*. In: Review. <https://doi.org/10.2139/ssrn.5253293>.
- Zhao, P., Peng, Z., 2008. Velocity contrast along the Calaveras fault from analysis of fault zone head waves generated by repeating earthquakes. *Geophys. Res. Lett.* 35, L01303. <https://doi.org/10.1029/2007GL031810>.
- Zhao, P., Peng, Z., Shi, Z., Lewis, M.A., Ben-Zion, Y., 2010. Variations of the velocity contrast and rupture properties of M6 earthquakes along the Parkfield section of the San Andreas fault. *Geophys. J. Int.* 180 (2), 765–780. <https://doi.org/10.1111/j.1365-246X.2009.04436.x>.
- Zor, E., Peng, Z., Ergin, M., Sandvol, E., Sevim, F., Tapırdamaz, M.C., Mach, P., Yalvaç, Ö., Tarancıoğlu, A., Koşma, M.K., Adeboboye, O., Ding, C., Açıkgöz, C., Büyüç, E., 2025. Dense seismic recordings of the 2023 Kahramanmaraş earthquake sequence in Southeastern Türkiye. *Seismol Res. Lett.* 96 (4), 2683–2697. <https://doi.org/10.1785/0220240152>.